Experimental Investigation and Crystal Plasticity Modelling of Dynamic Recrystallisation in Dual-Phase High Entropy Alloy During Hot Deformation

Zixin Zhou[1], Yuanming Huo [1*], Zhijun Wang [2*], Eralp Demir[3], Anqi Jiang[1], Zhenrong Yan [1], Tao He[1]

1. School of Mechanical and Automotive Engineering, Shanghai University of Engineering Science, Shanghai 101600, China;
2. State Key Laboratory of Solidification Processing, Northwestern Polytechnical University, Xi'an 710072, China;
3. Department of Engineering Science, University of Oxford, Parks road, Oxford OX1 3PJ, UK;

Abstract:

During high temperature processing, the Ni61Fe10Cr10Al17Mo2 high entropy alloy (HEA) often encounters problems with uneven stress distribution and grain size, which limits its industrial application. This study carried out high-temperature compression tests between 1100°C and 1200°C to investigate the behavior and influence of dynamic recrystallization (DRX) during thermal deformation. Using electron backscatter diffraction (EBSD) technology, microstructural changes at strain levels of 0.2 and 0.7 were thoroughly analysed, with particular attention to how temperature influences stress distribution and texture evolution, as well as differences in stress response between FCC and BCC phases. Additionally, thermodynamic analysis has been integrated into a dislocation density-based dual-phase crystal plasticity constitutive model, effectively describing the stress inhomogeneity and grain refinement during high-temperature processing. The findings demonstrate variations in the DRX mechanisms among different phases and illustrate their synergistic effects with deformation temperatures on microstructural evolution, thereby inducing localised stress concentrations. These insights provide valuable theoretical understanding of the thermal deformation behaviour in complex dual-phase alloy systems and offer a theoretical foundation for optimising processing parameters and enhancing the mechanical properties of HEAs.

Keywords: High entropy alloy, crystal plasticity, dual phase, dynamic recrystallisation, displacement density.

1. Introduction

High-entropy alloys (HEA) have attracted widespread attention for their outstanding properties[1]. Since CoCrFeMnNi HEAs were first proposed by Cantor et al. [2], single-phase HEAs with face-centred cubic (FCC), body-centred cubic (BCC), and hexagonal closed-packet (HCP) solid solutions have been extensively studied [3-7]. However, balancing strength and ductility in single-phase HEAs remains a significant challenge[5-7]. To address this issue, more dual-phase HEAs have been designed, and the use of dual-phase structures consisting of an FCC and a BCC / HCP phase is a promising approach to strike a balance between the strength and ductility of HEAs[5,8-10]. Among these, Jia et al. [9] proposed a Ni61Fe10Cr10Al17Mo2 HEA composed of the FCC phase and the BCC / B2 phase, showing a yield strength of 831 MPa and a 14.5% ductility.

Although HEA exhibit excellent room temperature properties, they are typically employed under high temperature conditions, making it crucial to understand their performance at elevated temperatures [11]. Research on thermal deformation behaviour has focused mainly on the AlxCoCrNiFe [12-14] and CoCrFeMnNi [15,16] series of HEA. Guo et al.[17] subjected the AlCoCrFeTi0.5Ni2.5 HEA to high temperature compression and observed strain softening above 700°C, yet the material maintained high strength, showing dense dislocation entanglements in the BCC phase. Jeong et al. [18]studied the hot deformation of CoCrFeMnNi HEA in the temperature range of 1173 to 1373 K and observed different dynamic recrystallisation (DRX) mechanisms in the FCC and BCC phases, leading to an uneven distribution of DRX grains. Stepanov et al. [19] performed an examination of the CoCrFeNiMn HEA microstructure under uniaxial compression in the temperature range 600 to 1100°C. Their findings indicated that discontinuous dynamic recrystallisation (DDRX) occurred along with the microstructural changes observed across all the temperatures analysed. However, research on the thermomechanical behaviour of the NiFeCrAl series alloys is limited. Wang et al. [20] determined the optimal hot working parameters for Ni61Fe10Cr10Al17Mo2 HEA during isothermal compression tests to be 1150-1175°C at 0.15-1.0 s^{-1}. Despite these findings, in-depth discussions on the stress contributions of different phases and the variations in DRX mechanisms within the NiFeCrAl series have not been thoroughly explored. Clarifying the mechanisms of high-temperature plastic deformation and the underlying

microstructural evolution is vital for metal forming processes such as hot rolling, forging, and extrusion [21]. This necessitates further investigation of the thermomechanical behaviour of dual-phase HEA through a combination of numerical predictions and experimental results.

Simulation methods such as molecular dynamics (MD), the finite element method (FEM), and the crystal plasticity finite element method (CPFEM) are effective in studying DRX behaviour and have been extensively used to investigate the thermomechanical deformation of dual-phase HEA. Rahul et al. [22]used FEM to investigate the distribution of the strain field and the flow of material in AlCoCrFeNi2.1, determining its optimal thermomechanical processing conditions. Qiao et al. [23] employed FEM and MD to explore the deformation mechanisms of Fe2Ni2CrAl under compression at various temperatures, analysing the nucleation mechanisms of dislocation at an atomic level at high temperatures. In predicting the plastic deformation behaviour of HEA, CPFEM is one of the most widely used and effective simulation tools[24-26]. Lu et al. [27] used CPFEM based on dislocation density to reveal the relationships between microstructural evolution, deformation mechanisms, and the cyclic deformation response in iHEA. Zhang et al. [28] constructed a polycrystalline representative volume element (RVE) that more closely matches the actual grain morphology and used CPFEM for in situ tensile modelling, revealing the reasons behind complex stress and strain distributions. However, these studies have primarily focused on using CPFEM for room temperature plastic deformation of single-phase HEA. There is a notable lack of research using CPFEM to explore the thermomechanical deformation of dual-phase HEA at high temperatures, which hampers progress in studying the evolution of DRX in HEA.

In this study, hot compression tests were performed at various temperatures with strain levels of 0.2 and 0.7 to investigate the DRX behaviour of the Ni61Fe10Cr10Al17Mo2 HEA. Microstructural characterisations revealed the evolution of stress and microstructure during the DRX process. Using the DRX evolution model proposed by An et al. [29]. and the crystal plasticity solver by Hardie et al.[30], a dislocation density-based CPFEM was developed to predict thermal deformation behaviours. The comparative analysis of the experimental and simulation results validates that the model precisely predicts stress softening, grain refinement, and dislocation annihilation induced by DRX. Additionally, this study meticulously examined the extent of DRX in dual-phase HEAs at different temperatures and the effects of DRX mechanisms in various phases on grain boundaries (GBs) and texture evolution.

2. Material and Experiment

2.1. Material and high-temperature compression

The material used in this work is a Ni61Fe10Cr10Al17Mo2 HEA, prepared using the vacuum induction melting process. To eliminate the influence of precipitate strengthening phases on the original material, the ingot was subjected to a heat treatment at 1200°C for 12 hours.

To study the rheological stress and microstructural evolution characteristics of the samples under different deformation parameters, high-temperature compression tests were conducted using a Gleeble-3500 thermo-simulation machine at downward pressures of 20% and 50%, corresponding to true strains of approximately 20% and 70%. The temperatures were set at 1100°C, 1150°C, and 1200°C, with strain rates at each temperature set to 0.001, 0.1, and 1 s^{-1}. After compression, the specimens were quenched in water to preserve the transient states during compression. Fig.1 is a diagram of the experimental procedure in this study, showing the specific rates of temperature change and heating times.

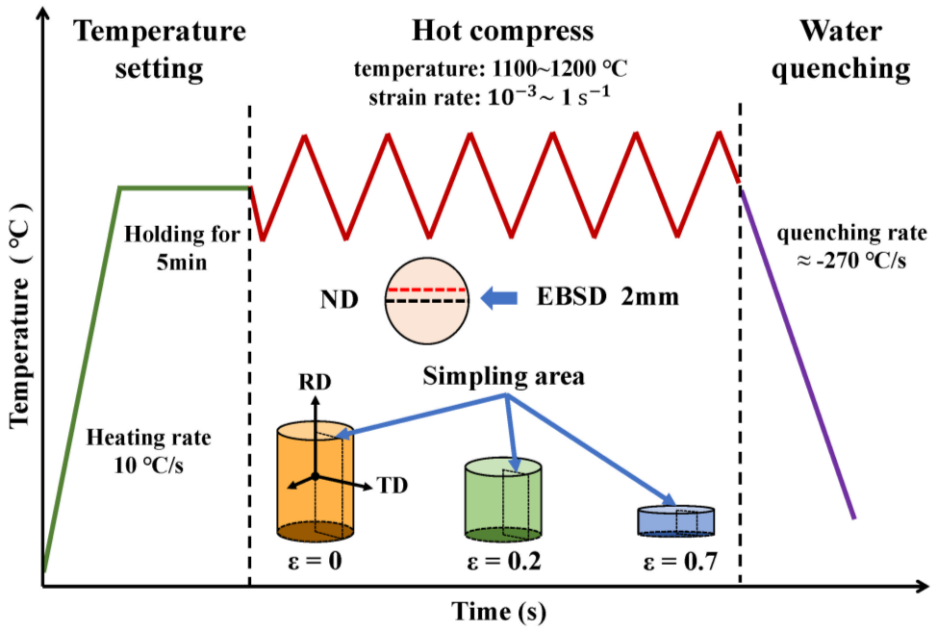

Fig 1 Schematic diagram of the experimental setup.

2.2. Microstructural Analysis

Cutting samples from the centre of compression specimens using electric discharge machining (EDM). The samples are initially wet ground using 800#, 1200#, 1500#, and 2000# sandpaper, followed by polishing with 1.5 and 1.0μm diamond pastes to achieve a mirror finish. Subsequently,

electrolytic polishing is performed in a solution consisting of 10% perchloric acid and 90% ethanol (vol%) to obtain high-quality surfaces. Electron backscatter diffraction (EBSD) analysis is performed using a FEI NOVA NANOSEM 450 field emission scanning electron microscope, with a configuration of a 2μm scan step, 20 kV voltage and a working distance of 15 mm. The collected area is 600μm × 600μm, and crystal orientation and texture analysis are performed using TSL OIM analysis software and the Matlab toolbox MTEX.

2.3. Initial microstructure results

The microstructure of Ni61Fe10Cr10Al17Mo2 HEA in its initial state (before deformation) is illustrated in Fig.2. EBSD analysis confirms the coexistence of FCC and BCC/B2 phases in the alloy, as depicted in the inverse pole figure (IPF) in Fig.2(a), where the larger grains mainly belong to the FCC phase. The BCC phase is distributed in a dendritic and interdendritic pattern, scattered within and along the boundaries of the FCC grains, demonstrating a noneutectic arrangement. Fig.2(b) displays the pole figures (PFs) for both phases, reflecting their crystallographic orientations. Fig.2(c) indicates that the average grain size of the FCC phase is approximately 293 μm, while the grains of the BCC phase are significantly finer, averaging 23.7 μm.

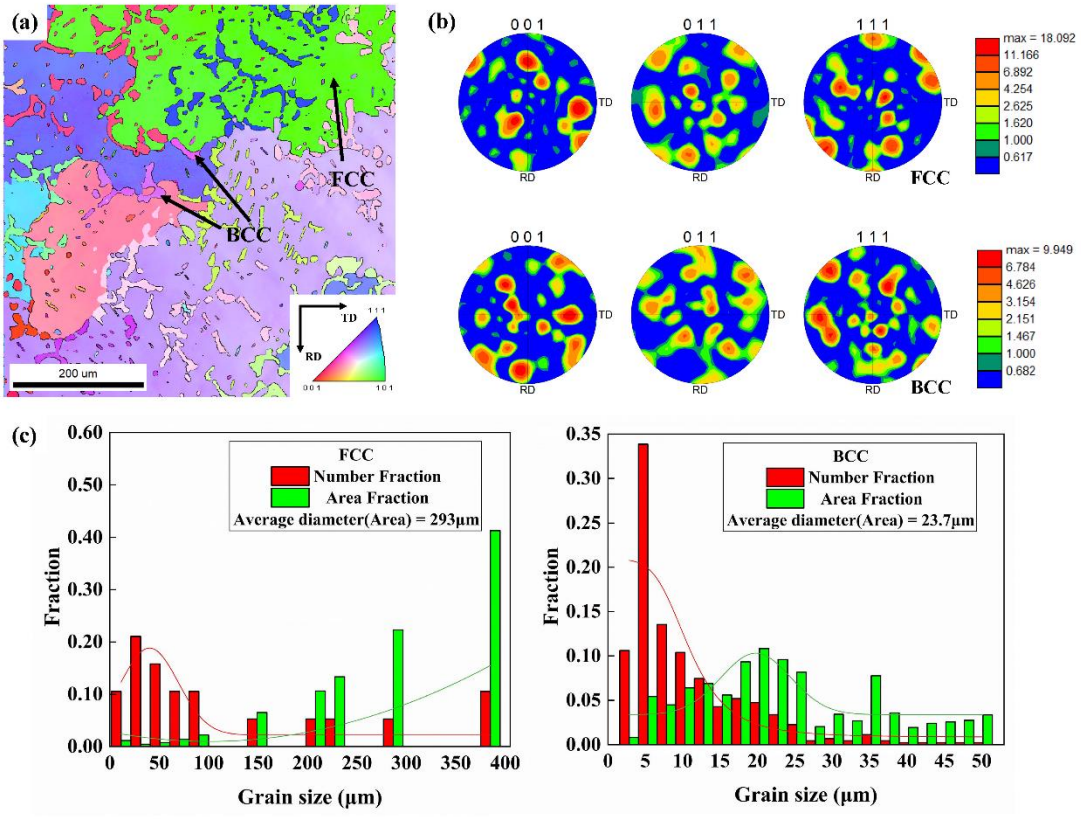

Fig. 2 (a) EBSD IPF map. (b) PF of the FCC phase and the BCC phase. (c) The grain sizes of the FCC phase and the BCC phase.

2.4. Phase Transformation of FCC and BCC Phases After Deformation

Furthermore, to elucidate the size, morphology, and distribution of the phases more comprehensively, Fig.3 presents the phase distribution maps before and after deformation. In the initial state, the area fraction of the FCC phase is 0.837, while that of the BCC phase is 0.163. After high-temperature deformation to a strain of 0.7 at three different temperatures, the volume fractions of the FCC and BCC phase remain essentially unchanged from their initial state, indicating that there is no phase transformation during high-temperature deformation of the material.

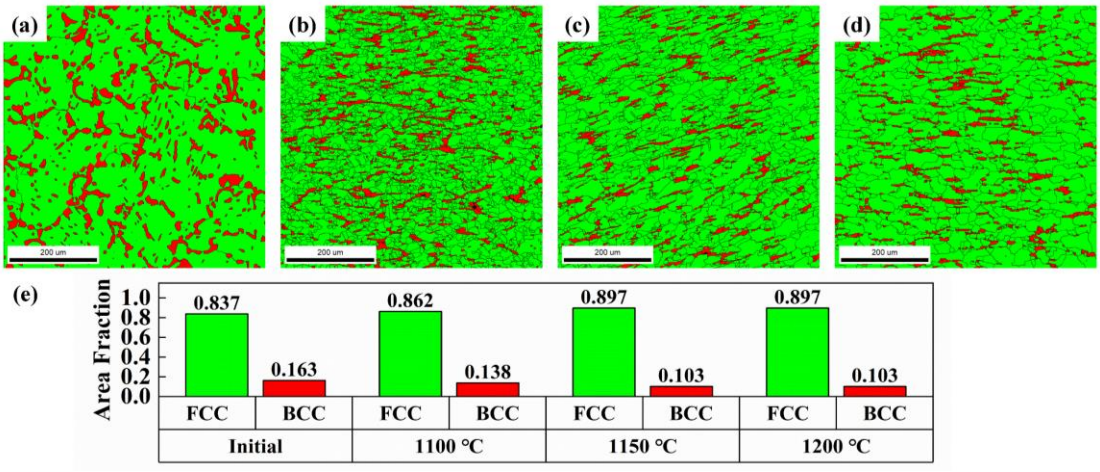

Fig 3 Phase distribution maps at (a)the initial state, (b)1100°C, (c)1150°C, and (d)1200°C. (e) Area fractions of the FCC phase and BCC phase in different states.

3. Modelling and Simulation Methods

3.1 Crystal-Plasticity Modelling

3.1.1 Finite deformation framework

In the finite-strain framework of elastoplastic deformation, the total deformation gradient $\boldsymbol{F}$ denotes the mapping of material points from the reference configuration to the current configuration. It is multiplicatively decomposed into elastic $\boldsymbol{F_e}$ and plastic $\boldsymbol{F_p}$ components [31], with the constraint $\boldsymbol{det}(\boldsymbol{F_p}) = 1$[1]:

$$\boldsymbol{F} = \boldsymbol{F_e}\boldsymbol{F_p} \tag{1}$$

The generalised Hooke's law establishes the correlation between the elastic Green-Lagrange

[1] Scalar quantities are indicated with normal fonts. Vector and tensor quantities of higher order are denoted with small and capital bold fonts, respectively: $\boldsymbol{a} = a_i$, $\boldsymbol{A} = A_{ij}$, and $\mathbb{C} = \mathbb{C}_{ijkl}$.

strain tensor $\boldsymbol{E}_{\mathbf{e}}$ and the Cauchy stress tensor S through an elastic stiffness tensor, represented as:

$$\boldsymbol{S} = \mathbb{C}: \boldsymbol{E}_{\mathbf{e}} \tag{2}$$

where $\mathbb{C}$ is a fourth-order anisotropic elastic stiffness tensor at the deformed configuration. The elastic Green-Lagrange strain tensor $\boldsymbol{E}_{\mathbf{e}}$ is defined as follows:

$$\boldsymbol{E}_{\mathbf{e}} = \frac{1}{2}(\boldsymbol{F}_{\boldsymbol{e}}^{T}\boldsymbol{F}_{\boldsymbol{e}} - \boldsymbol{I}) \tag{3}$$

where $\boldsymbol{I}$ is the second-order identity tensor. The evolution law for the plastic deformation gradient is as follows:

$$\dot{\boldsymbol{F}}_{\boldsymbol{p}} = \sum_{\alpha}^{N_S} \dot{\gamma}^{\alpha} \cdot (\boldsymbol{m}_{\mathbf{0}}^{\boldsymbol{\alpha}} \otimes \boldsymbol{n}_{\mathbf{0}}^{\boldsymbol{\alpha}})\, \boldsymbol{F}_{\boldsymbol{p}} \tag{4}$$

is the plastic velocity gradient, $\dot{\gamma}^{\alpha}$ is the plastic shearing rate on the αth slip system, $\boldsymbol{m}_{\mathbf{0}}^{\boldsymbol{\alpha}}$ and $\boldsymbol{n}_{\mathbf{0}}^{\boldsymbol{\alpha}}$ are slip direction and slip plane normal, respectively, of the slip system α at the intermediate configuration [32]; It should be noted that, due to the absence of deformation twinning and phase transformation in the investigated HEA at high-temperatures, the primary plastic deformation mechanism is governed by dislocation slip, where N_S is the total number of sliding systems in the material.

3.1.2 Dislocation-density-based crystal plasticity constitutive model

The crystal plasticity constitutive model used in this research is based on dislocation density. The relationship between the plastic shearing rate $\dot{\gamma}^{\alpha}$ and the average velocity v^{α} can be expressed through Orowan's equation[33]:

$$\dot{\gamma}^{\alpha} = \rho^{\alpha} b v^{\alpha} \tag{5}$$

where ρ^{α} is the mobile dislocation density of the slip system α, and b is the Burgers vector. the average velocity v^{α} as [34]:

$$v^{\alpha} = v_0 exp\left(\frac{-\Delta G}{k_B T}\right) \tag{6}$$

k_B is the Boltzmann's constant, and T is the absolute temperature, v_0 is the reference dislocation slip velocity; ΔG is the average activation energy required to overcome the short-range barrier, can be expressed as:

$$\Delta G = \Delta Q \left[1 - \left(\frac{|\tau^{\alpha}|}{\tau_c^{\alpha}}\right)^{p}\right]^{q} \tag{7}$$

where ΔQ is activation energy for mobile dislocations to overcome short-range barrier, p and q are the material parameters related to the barrier profile, $\tau^{\alpha}$is the resolved shear stress of

the α slip system which can be calculated by Schmid law[35], and τ_c^{α} is the critical resolved shear stress(CRSS). Insert Eq.(7) and (8) into Eq.(6) to obtain:

$$\dot{\gamma}^{\alpha} = \rho^{\alpha} b v_0 exp\left(-\frac{\Delta Q}{k_B T}\left[1-\left(\frac{|\tau^{\alpha}|}{\tau_c^{\alpha}}\right)^{p}\right]^{q}\right) sgn(\tau^{\alpha}) \tag{8}$$

It should be noted that, in crystal plasticity, most implicit schemes are based on the Newton-Raphson "predictor-corrector" method, commonly used to minimise stress errors[36,37]. However, the effectiveness of conventional solvers is limited by their narrow convergence intervals, especially when dealing with materials characterised by nonlinear slip laws and low sensitivity to strain rate. Hardie et al.[30] proposed that the efficiency of the solution process can be accelerated by utilizing the reverse form of the slip law, where shear stress τ_c^{α} is expressed as a function of plastic shear strain rate, transforming the equation from $\dot{\gamma}^{\alpha} = f(\tau)$ to $\dot{\gamma}^{\alpha}: \tau = f(\dot{\gamma}^{\alpha})$.

The inverted form of the enthalpy-based slip law is:

$$\tau_v^{\alpha} = \left(\tau_c^{\alpha}\left[1-\left(-\ln\left(\frac{|\dot{\gamma}^{\alpha}|}{\rho^{\alpha} b v_0}\right)\frac{k_B T}{\Delta Q}\right)^{\frac{1}{q}}\right]^{\frac{1}{p}}\right) \mathrm{sgn}(\dot{\gamma}^{\alpha}) \tag{9}$$

The derivatives of Eq. (9) with respect to shear stresses solved in the forward case is:

$$\frac{d\dot{\gamma}^{\alpha}}{d\tau^{\alpha}} = \frac{|\dot{\gamma}^{\alpha}|\Delta Q q p}{k_B T \tau_c^{\alpha}}\left[1-\left(\frac{|\tau^{\alpha}|}{\tau_c^{\alpha}}\right)^{p}\right]^{q-1}\left(\frac{|\tau^{\alpha}|}{\tau_c^{\alpha}}\right)^{p-1} \tag{10}$$

and the derivative of Eq. (10) with respect to the slip rates solved in the reverse case is:

$$\frac{d\tau_v^{\alpha}}{d\dot{\gamma}^{\alpha}} = \frac{k_B T \tau_c^{\alpha}}{|\dot{\gamma}^{\alpha}| Q q p}\left[1-\left(-\ln\left(\frac{|\dot{\gamma}^{\alpha}|}{\rho^{\alpha} b v_0}\right)\frac{k_B T}{\Delta Q}\right)^{\frac{1}{q}}\right]^{\frac{1-p}{p}}\left(-\ln\left(\frac{|\dot{\gamma}^{\alpha}|}{\rho^{\alpha} b v_0}\right)\frac{k_B T}{\Delta Q}\right)^{\frac{1-q}{q}} \quad \text{for } |\dot{\gamma}^{\alpha}| > 0 \tag{11}$$

The slip shear rate of the slip system α including temperature effects is expressed by a modified Orowan equation [24,33]:

$$\tau_c^{\alpha}(\dot{\varepsilon}, T) = \tau_0^{\alpha} + \tau_{HP}^{\alpha}(\dot{\varepsilon}, T) + \tau_{for}^{\alpha}(\dot{\varepsilon}, T) \tag{12}$$

is contributed by the intrinsic frictional resistance τ_0^{α} and the other hardening sources, τ_{HP}^{a} is a barrier term that reflects the effect of grain size on metal yield stresses, as described by the Hall-Petch relationship[38]. This relationship emphasises the role of grain boundaries (GBs) in obstructing dislocation slip, which significantly impacts the strength of nanocrystalline materials.

$$\tau_{HP}^{a}(\dot{\varepsilon}, T) = \frac{k_{HP}\mu\sqrt{b}}{\sqrt{d}} \tag{13}$$

where d is the grain size, k_{HP} is a parameter influenced by the CRSS of the material, and μ is the shear modulus. τ_{for}^{α} reflects the impact on slip resistance evolution from the accumulation of forest dislocation density ρ_{for}^{a}, as characterised by the traditional Taylor's law. The geometric factor χ is typically represented in the form of a diagonal matrix[39], here, it is simplified to a value of 0.25:

$$\tau_{for}^{a}(\dot{\varepsilon},T)=\mu b\sqrt{\underbrace{\chi^{2}\rho_{\text{for}}^{a}}_{\text{cut-through}}} \tag{14}$$

The evolution of the slip system for the overall dislocation density $\dot{\rho}^{\alpha}$ is:

$$\dot{\rho}^{\alpha}=\left(k_{1}\sqrt{\rho_{\text{for}}^{\alpha}}-k_{2}(\dot{\varepsilon},T)\rho^{\alpha}\right)|\dot{\gamma}^{\alpha}| \tag{15}$$

The relationship between the rate-insensitive coefficient for dislocation storage k_1 and coefficient for dislocation dynamic recovery $k_2(\dot{\varepsilon},T)$ is[40]:

$$k_{2}(\dot{\varepsilon},T)=k_{1}\frac{\xi b}{g^{a}}\left(1-\frac{k_{B}T}{D^{a}(b)^{3}}\ln\frac{\dot{\varepsilon}}{\dot{\varepsilon}_{0}}\right) \tag{16}$$

where $\xi, g^{a}, D^{a}, \dot{\varepsilon}_{0}$ are dislocation interaction parameter, effective activation enthalpy, drag stress and reference strain rate.

3.1.3 The effect of DRX on dislocation density

DRX decreases dislocation density by eliminating and rearrangement of dislocations. Integrating this mechanism into Eq.(15) yields the modified dislocation density evolution equation:

$$\dot{\rho}^{\alpha}=\left(k_{1}\sqrt{\rho_{\text{for}}^{\alpha}}-k_{2}(\dot{\varepsilon},T)\rho^{\alpha}\right)|\dot{\gamma}^{\alpha}|-\dot{\rho}_{\text{DRX}}^{\alpha} \tag{17}$$

$\dot{\rho}_{DRX}^{\alpha}$ represents the rate of dislocation density evolution caused by DRX, with dislocation density evolving with deformation and gradually approaching saturation. A series of experimental analyses of DRX [29,41] have resulted in a numerical formula that reflects this mechanism, leading to the proposition of the following equation for DRX-induced dislocation density evolution:

$$\dot{\rho}_{DRX}^{\alpha}=\frac{k_{DRX}}{\mu b^{2}}\left(1-\frac{d}{d_{0}}\right)\dot{W}_{p}\left(1-\frac{\rho_{\min}}{\rho^{\alpha}}\right)^{2} \tag{18}$$

where k_{DRX} is the evolution parameter for dislocation density, $\rho_{\min}$ is the critical residual dislocation density in grains after DRX. In Eq.(18), the evolution of dislocation density due to DRX includes both microstructure evolution and energy transformation during deformation. The grain size serves as the primary metric for quantifying the impact of DRX on microstructural changes. Throughout the DRX process, as plastic deformation progresses, grains are progressively refined,

evolving towards a saturation size d_s. Moreover, once the grain size reaches this saturation point, the DRX process halts and, consequently, the evolution of dislocation density induced by DRX ceases. The equation for grain size evolution is formulated as follows:

$$\dot{d} = \delta \frac{k_d}{\mu} \dot{W}_p (d_s - d) \tag{19}$$

$\dot{W}_p$ is the rate of plastic work done obtained by the double dot product of the stress tensor σ and the plastic strain tensor $\dot{\varepsilon^P}$, representing the energy generated in plastic deformation. δ s the nucleation indicator of DRX.

In hot deformation processes, significant plastic deformation or dislocation activity facilitates the nucleation and subsequent growth of DRX. Thus, the critical values of accumulated plastic strain or dislocation density are deemed indicative of the onset of DRX. It is essential, however, to recognise that for metals with diverse textural characteristics or even within the same specimen, a uniform critical strain may not reliably predict the onset of DRX. Research by Rittel et al. [42] has elucidated that the genesis of DRX is intrinsically related to dynamic energy stored throughout the deformation process. An et al.[29]have advocated for the delineation of DRX nucleation using an energy threshold criterion, stipulating that DRX commences when the energy sequestered within the crystal lattice exceeds a predetermined energy threshold ϕ_0:

$$\delta = \begin{cases} 1 & \phi > \phi_0 \\ 0 & \phi \leq \phi_0 \end{cases} \tag{20}$$

ϕ is the plastic work stored in the lattice, as derived from the equation $\phi = (1 - \beta) W_p$. The Taylor-Quinney coefficient β excludes the portion of the plastic work W_p dissipated as heat energy. When it exceeds the critical energy threshold ϕ_0, the indicator δ equals 1, signifying the nucleation of DRX.

3.2 Dual-phase RVE model and boundary conditions

Simulations of crystal plastic compression deformation were conducted by integrating the user material subroutine (VUMAT) into the finite element software ABAQUS. A polycrystalline RVE was created with DREAM.3D[43] based on the volume fractions of the FCC and BCC phases and the crystal orientations, resulting in models with 3375, 8000,27000 and 64000 C3D8 elements as depicted in Fig.4(a). The volume fraction of the BCC phase was set at 0.1, with 0.9 located in the GBs, generated in proportion to the actual EBSD-measured phase grain sizes, accurately reflecting the structure of the material.

Studies on model optimisation reveal that polycrystalline RVE simulations are insensitive to the number of grains, showing that as few as 50 grains can adequately represent the macroscopic homogenised deformation of polycrystalline alloys[44,45]. However, in terms of the number of elements, polycrystalline RVE simulations exhibit high sensitivity, where finer meshes yield better accuracy[46,47], and differences diminish as a certain mesh density is reached [25]. Fig.4(b) shows that beyond 27000 elements, there is almost no difference in the macroscopic stress-strain curves, but at the yield point, more elements align more closely with actual experimental data. Fig.4(c) further illustrates the stress comparison curves for FCC and BCC structures at the microscale with different mesh numbers, including Von Mises stress and axial stress. The compressive axial stress consistently exceeds the Von Mises stress, and this difference becomes more pronounced at higher strains. The results for 27,000 and 64,000 meshes are quite consistent, clearly reflecting this disparity. Therefore, to optimize computational accuracy, the polycrystalline model was meshed using 27000 (30×30×30) elements, containing 18 FCC phase grains and 449 BCC phase grains.

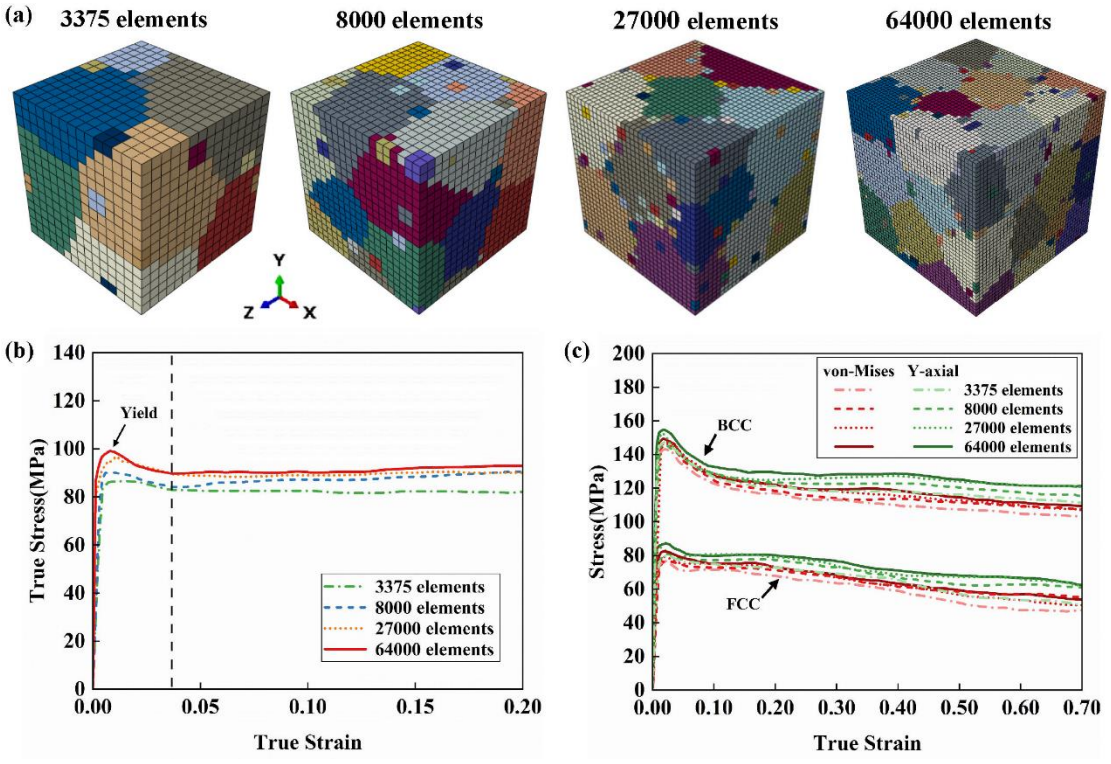

Fig 4 (a) RVE with different mesh refinements. (b) True stress-strain curves based on different mesh refinements. (c) Micro scale stresses curves on different mesh refinements.

The constructed dual-phase RVE is shown in Fig.5(a). Boundary conditions were applied to this model as shown in Fig.5(b), where the Y-direction degree of freedom ($U_Y = 0$) was set for the

bottom surface ABCD as a fixed face, the line AD constrained by the X-direction degree of freedom ($U_X = 0$), and the line DC by the Z-direction degree of freedom ($U_Z = 0$) to prevent rigid body displacement during compression. The load was applied to the top surface EFGH, investigating the model's compression deformation at temperatures of 1100℃, 1150℃, and 1200℃, with high-temperature diffusion not considered and temperature maintained constant during the deformation process.

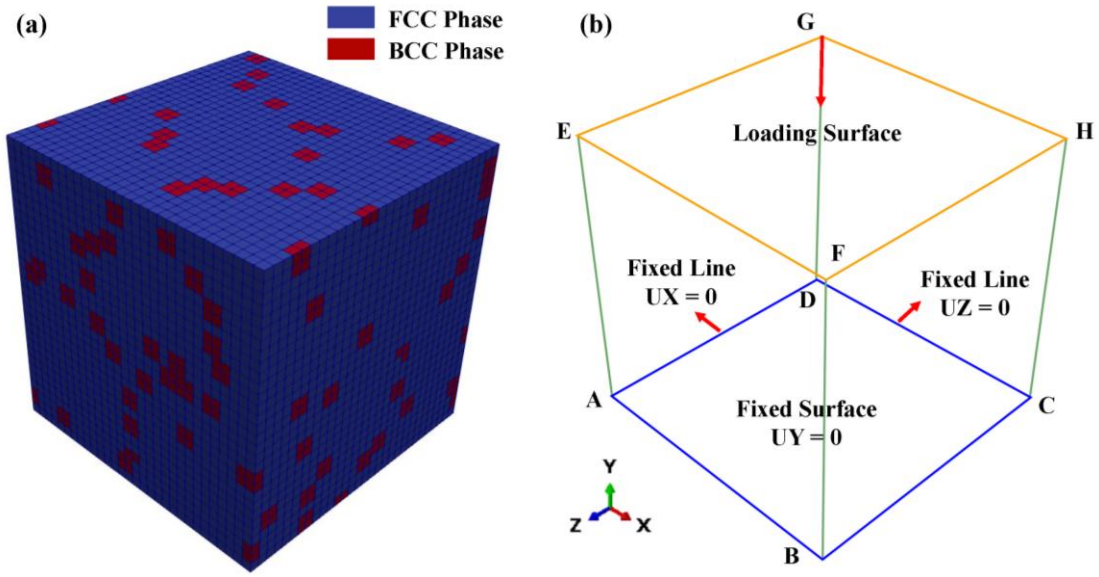

Fig. 5 (a) Dual phase RVE. (b) Schematic of the boundary conditions applied to the RVE.

3.3 Constitutive Model Parameters

The grain size and dislocation density parameters were quantified through EBSD analysis. The initial dislocation density, ρ_0^{α}, was experimentally determined to be 11.5 μm^{-2}, while the minimum dislocation density ρ_{min}^{α} after DRX was 5 μm^{-2}. The parameters p, q are fitting parameters used to adjust the temperature sensitivity of the constitutive model, which in this work are set to 0.96 and 1.2, respectively, based on the analysis of experimental data. Subsequently, hardening-related parameters k_1, ξ, g^a, D^a, $\dot{\epsilon}_0$ were derived by fitting experimental stress-strain curve data.

In this study, the Young's modulus E of the Ni61Fe10Cr10Al17Mo2 HEA was measured to be 160.02 GPa, and the Poisson's ratio u, based on the research by Jia et al.[9], was determined to be 0.43, with the Burgers vector b reported as 0.255 nm. The shear modulus G was calculated using the formula $G = E/[2(1+u)]$. For the FCC phase, the elastic constants by Gao and Wang et al.[24,48] are referenced, while for the BCC phase, the elastic constants C_{11}, C_{12}, andC_{44}were

calculated based on the variations in Young's modulus and Poisson's ratio between different phases[49,50]. Simulations were conducted at temperatures of 1100°C, 1150°C, and 1200°C, during which the parameters k_{HP} and k_{DRX} varied according to phase and temperature[9,29]. These parameters were differentiated on the basis of the described dependencies, with k_{DRX} calculated as $1.5 + 7.5 \times 10^{-3} \times (T - 1100)$, resulting in values of 1.5, 1.875, and 2.25, respectively. The parameters of the related material of the HEA are listed in Table 1. For the BCC phase, except for the parameters specified in Table 2, all other parameters are consistent with those of the FCC phase.

Table 1 Constitutive parameters of the FCC phase.

Parameter	Describe	Value and unit	Origin
C_{11}	Elastic moduli parameter	271×10^3 MPa	[24,48]
C_{12}	Elastic moduli parameter	175×10^3 MPa	[24,48]
C_{44}	Elastic moduli parameter	189.3×10^3 MPa	[24,48]
v_0	Reference dislocation glide velocity	1×10^{-4} m/s	[27]
ΔQ	Activation energy	3.5×10^{-19} J	[27]
k_B	Boltzmann constant	1.38×10^{-23} J/K	[27]
b	Magnitude of Burgers vector	0.255 nm	[9]
p, q	Exponents in glide velocity	0.96/1.2	(This work)
τ_0^α	Peierls stress	10 MPa	[9]
k_{HP}	Hall-Petch slope	60 MPa·μm$^{1/2}$	[9]
k_1	Hardening constant	733	(This work)
ξ	Dislocation interaction parameter	0.9	(This work)
g^a	Effective activation enthalpy	1.5×10^{-3}	(This work)
D^a	Drag stress	300	(This work)
$\dot{\epsilon_0}$	Reference slip rate	1×10^{-3}	(This work)
d_0	Initial grain size	293 μm	(This work)
d_s	Saturation grain size	10 μm	(This work)
ϕ_0	The threshold of stored energy density for DRX	95 mJ/mm^3	[29]
k_d	Grain evolution parameter	2×10^3	[29]
ρ_0^α	Initial dislocation density	11.5 μm^{-2}	(This work)
ρ_{min}^α	The dislocation density after DRX	5 μm^{-2}	(This work)

Table 2 BCC phase constitutive parameters.

Parameter	Describe	Value and unit	Origin
C_{11}	Elastic moduli parameter	315.5×10^3 MPa	[49,50]
C_{12}	Elastic moduli parameter	215.4×10^3 MPa	[49,50]
C_{44}	Elastic moduli parameter	148.7×10^3 MPa	[49,50]
k_{HP}	Hall-Petch slope	21 MPa·μm$^{1/2}$	[9]
d_0	Initial grain size	23.7 μm	(This work)

The RVE was compressed to a strain of 0.7 at temperatures of 1100°C, 1150°C, and 1200°C, with strain rates of 0.001 s^{-1}, 0.1 s^{-1} and 1 s^{-1}, respectively. Fig.6 compares the experimental and simulated true stress-strain curves of the Ni61Fe10Cr10Al17Mo2 HEA under hot compression. The initial decrease in stress values at the start of plastic deformation is attributed to the consumption of a significant number of dislocations due to the generation and evolution of DRX in the first stage[20,51], while the second stage of DRX-induced softening, occurring near a strain of 0.2, leads to a continuous decline in stress. The crystal plasticity simulation captures this phenomenon, and showing a generally good agreement with the experimental results indicates that DRX is the primary cause of material softening at high temperatures. Notably, in Fig.6(b), the simulation accuracy at 1150°C is better than at 1100°C and 1200°C. At a strain rate of 0.001 s^{-1}, discrepancies between the simulated and actual values arise when the strain exceeds 0.5. The actual stress remains relatively constant with temperature at low rates, at a strain rate of 1 s^{-1}, the observed stress drop at the onset of plastic deformation is not significantly captured in the simulation. It is evident that the best agreement is achieved when the strain rate is 0.1 s^{-1} at all temperatures. It should also be noted that the minimum strain required to achieve significant softening effects varies with temperature; experimental and simulation results show that as the temperature increases, the softening from the second stage of DRX occurs increasingly later.

To further confirm and establish the dependability of the crystal plasticity model, both the correlation coefficient (R) and the root mean square error (RMSE) were utilised to assess the stress-strain curves:

$$\mathrm{RMSE} = \sqrt{\frac{1}{N}\sum_{i=1}^{N}(x_i - y_i)^2} \tag{21}$$

x_i is the stress value obtained in the experiment and y_i is the stress value obtained in the simulation, acquisition of 10 data points at each temperature. The calculated R and RMSE are shown in Table 3.

Table 3 R and RMSE for different temperatures

	1100	**1150**	**1200**
R	0.984	0.991	0.976
RMSE	5.82	4.56	6.79

Across the three temperature conditions, the R values exceeded 0.97, indicating a high

correlation between the simulated and experimental values with minimal error. At 1150°C, the R value reached 0.006, and the RMSE was 4.56, presenting the best fit to the experimental data, the RMSE values at 1100°C and 1200°C are also low. The overall correlation coefficient map is depicted in Fig.6(d), illustrates that the crystal plasticity model is capable of predicting the key attributes of the Ni61Fe10Cr10Al17Mo2 HEA with the level of precision required for accurate simulations.

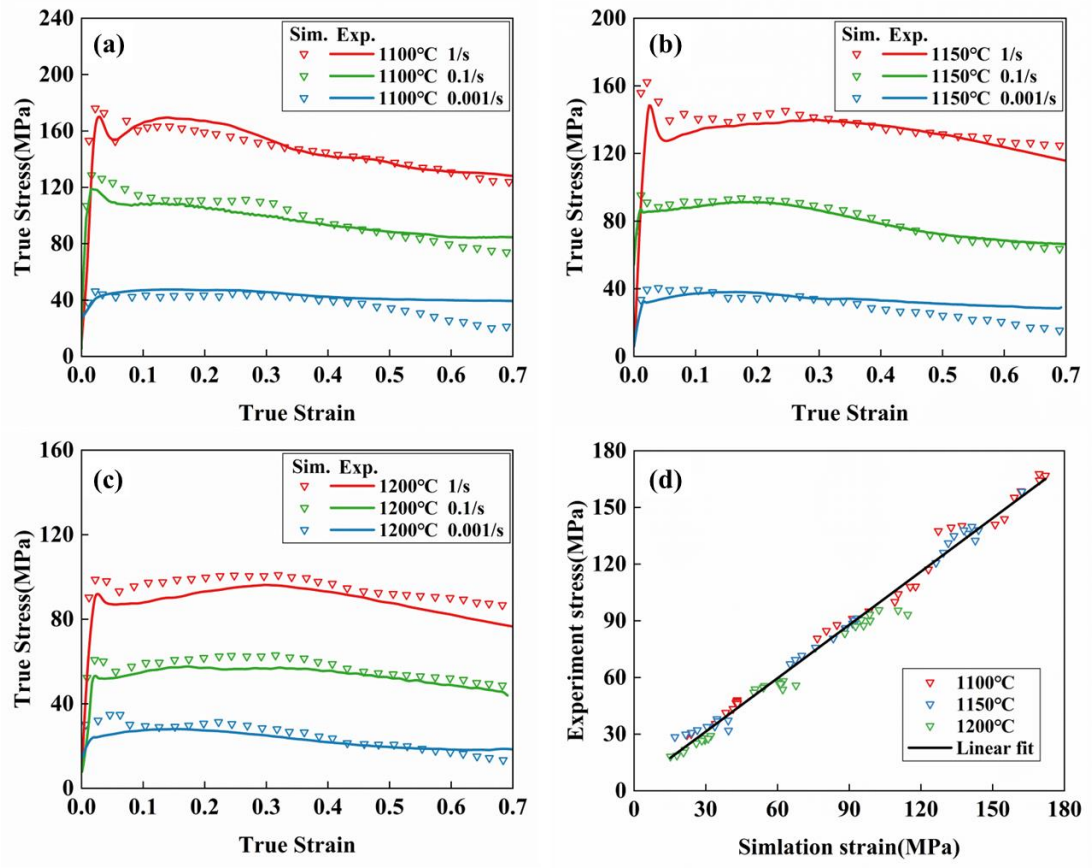

Fig. 6 Comparison of experimental data and simulation results for true stress-strain curves at (a)1100°C, (b) 1150°C, and (c) 1200°C, (d) Correlation coefficient map.

4. Results and Discussion

4.1 Variations in hardening rate and stress concentration during DRX

Research on Ni61Fe10Cr10Al17Mo2 HEA during high-temperature deformation has revealed a complex interaction between the hardening rate of work and the strain. At a temperature of 1150°C, the variations in the hardening rate displayed in Fig.7 align with the phenomena observed in Fig.6(b): a significant softening mechanism occurs when the strain reaches approximately 0.2, during which the hardening rate transitions from positive to negative, clearly indicating a close connection

between DRX-induced softening and strain.

Initially, DRX occurring in the first phase leads to a reduction in the work hardening rate. As plastic deformation progresses, however, the work hardening rate continues to rise and remains above zero. At the same time, the dislocation density increases with plastic deformation and gradually saturates in areas of concentration of strain. Fig.7(a) illustrates the distribution of von Mises stress, highlighting the variations in hardening contributions between different phases, particularly in region P1 where the stress in the BCC phase is noticeably higher than that in the FCC phase, and the stress at the GBs is higher than within the grain interiors. This phenomenon is observed in the stress-strain curves depicted in Fig.7(b) and is generally attributed to differences in crystal structures, resulting in different deformation modes of the phases and generating larger strain gradients[52,53]. This further indicates that the grains in the BCC phase are not only smaller but also harder. Additionally, due to the microstructural arrangement of the BCC phase surrounding the FCC phase, these areas of high stress concentration are primarily located near the phase boundaries. However, in the dislocation density distribution maps, the correlation between dislocation density and stress distribution in region P1 is not significant.

When the true stress exceeds 0.2, a stress drop occurs and the work hardening rate falls further to negative values revealing itself as a strain softening effect. This rapid decline in hardening rate marks the nucleation and expansion of DRX, as new areas of stress concentration begin to form with the increase in the amount of deformation. Under high strain rates, this localised stress concentration manifests itself as shear bands[29], while under the low strain rate conditions of this study, the observed stress concentrations appear primarily around the slip bands in region P2 [54]. These slip bands traverse the grain interiors, displaying lower dislocation density and stress levels on the bands, while high stress concentrations emerge at the edges of the bands. This indicates that the softening effects and hardening mechanisms of DRX are not balanced in different strain regions.

The stress concentrations produced at the edges of the slip bands gradually replace the original stress concentration patterns at the GBs. The crystal plasticity model accurately captures the dynamic changes in the hardening rate caused by DRX.

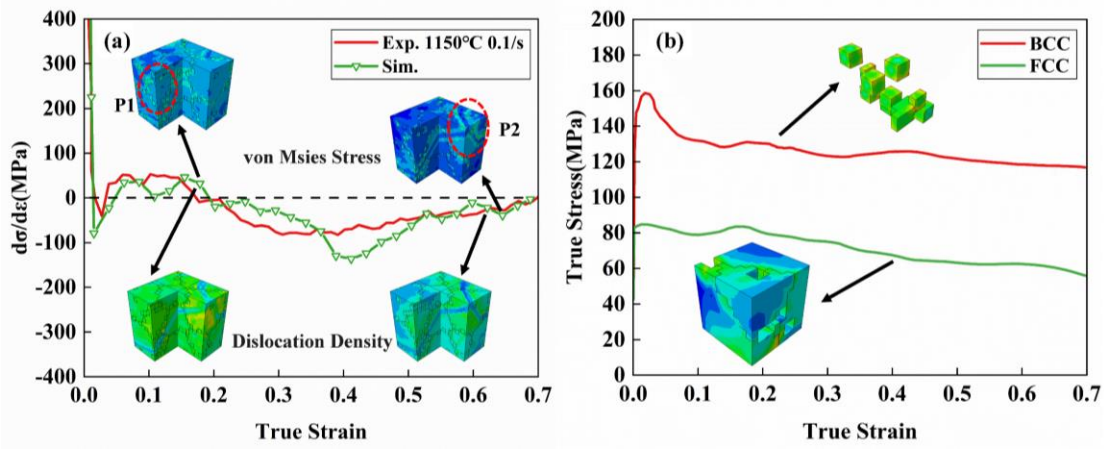

Fig. 7 (a) Comparison of experimental data and simulation results for work hardening rate curves. (b) Simulation of stress-strain curves for the FCC and BCC phases at 1150°C.

4.2 Predicting temperature-affected DRX behaviour through CPFEM models

4.2.1 Experimental analysis of microstructural characteristics

To further investigate the influence of varying temperatures on the DRX mechanism and its effect on stress, grain size, and dislocation density, Fig.8 shows the IPF and grain orientation spread (GOS) map for high-temperature compression up to a strain of 0.2 and 0.7 below 1100°C, 1150°C, 1200°C.

In Figs. 8(a1)-(f1), GOS was utilised to assess the distribution of DRX, quantifying the average orientation difference between grains to characterise the dispersion of grain orientation. Grains with GOS values ranging from 0 to 1° were identified as having undergone DRX, while those with GOS values above 1° were classified as unrecrystallized, deformed grains. It is evident that the distribution of DRX varies significantly under different levels of strain and temperatures.

As illustrated in Figs. 8(a), (c), and (e), DRX is observed at a strain of 0.2, particularly at 1150°C where significant grain refinement is evident, the proportion of DRX, f_{DRX}, reaches 40.7%. This phenomenon can be attributed to elevated temperatures that enhance atomic diffusion rates, which, in turn, promote the nucleation and growth of new grains. The formation of these new grains typically results in a reduction in dislocation density and refinement of the grain structure [41]. Although the most pronounced DRX process occurs at 1150°C, where the FCC phase grains are refined into numerous equiaxed grains with reduced sizes, there are still large unrecrystallized grains with subgrain boundaries alongside smaller DRX grains. At this temperature, the f_{DRX} for the FCC

phase is 43.9%, while the f_{DRX} for the BCC phase is 8.6% nearly non-existent, indicating that grain refinement is uneven and the DRX process is not yet complete at a strain of 0.2.

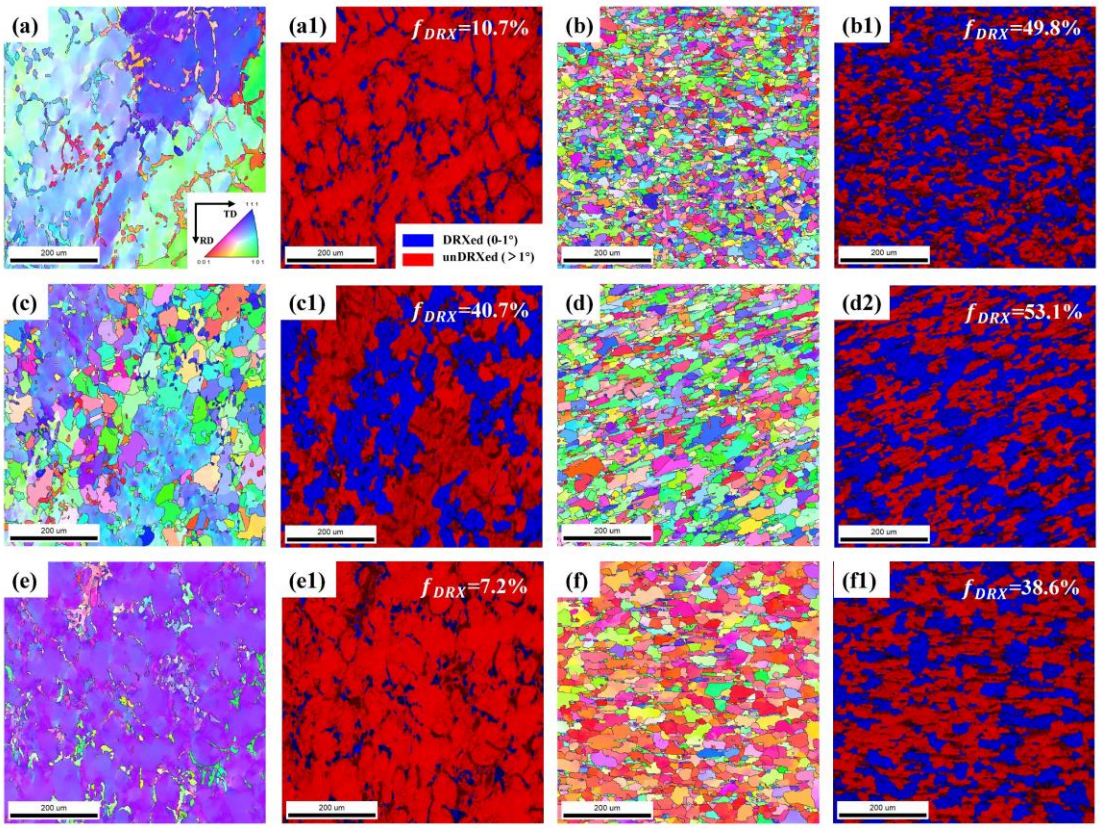

Fig. 8 IPF maps and GOS maps of Ni61Fe10Cr10Al17Mo2 HEA at different temperatures and strains: (a-a1) 1100°C, ε = 0.2; (b-b1) 1100°C, ε = 0.7; (c-c1) 1150°C, ε = 0.2; (d-d1) 1150°C, ε = 0.7; (e-e1) 1200°C, ε = 0.2; (f-f1) 1200°C, ε = 0.7.

At temperatures of 1100°C and 1200°C, as shown in Fig.8(a) and (e), temperature significantly affects the DRX driving forces. f_{DRX} are respectively 10.7% and 7.2%, lower than 1150°C. At 1100°C, the lower temperature decelerates the migration and reorganisation of the subgrain boundaries, requiring more accumulation to reach the critical strain for DRX. The IPF map shows numerous subgrain boundaries within the FCC phase, where increased local dislocation density does not fully reorganise into new grains, leading to slower and less pronounced DRX. On the contrary, at 1200°C, the higher temperature accelerates the migration of GBs [55]. Rapid elimination and reorganisation of subgrain boundaries aid in the migration and coalescence of boundaries, and the nuclei formed at these boundaries grow rapidly. This rapid growth leads to the fusion of new grains, as reflected in the IPF map by FCC grains with nearly identical crystal orientations merging into large grains. Other studies [56] have also shown that the initiation of DRX is highly sensitive to

temperature. These findings indicate that temperature primarily dictates grain refinement or growth trends by affecting DRX nucleation and boundary migration rates, resulting in significant variations in the critical strain levels for DRX during high temperature deformation at different temperatures.

Upon reaching a true strain of 0.7, significant DRX was observed at all temperatures. The original grains were elongated perpendicular to the compression direction and surrounded by numerous fine equiaxed DRX grains in the GBs, forming a "necklace" structure [20] as shown in Fig.8(f). At 1100°C, the grains are more uniformly equiaxed, f_{DRX} reaches 49.8%, indicating a thorough DRX process. The DRX process at this strain level is more pronounced due to increased plastic deformation and dislocation accumulation, resulting in notable grain refinement and uniform distribution. At 1150°C, since the DRX process had already significantly occurred at strain of 0.2, the f_{DRX} Only increases to 53.1%, but remains higher than the 38.6% observed at 1200°C, indicating that higher temperatures result in a lower volume fraction of complete DRX. Notably, the f_{DRX} in the BCC phase increases to 44.1% at a strain of 0.7, less than the 54.2% in the FCC phase, indicating different DRX mechanisms between phases.

The impact of temperature on DRX is particularly evident in the changes in grain size. To further investigate the effect of temperature on DRX and the differences in DRX proportions between two phases, Fig.9 displays the variations in grain size during the DRX deformation process.

Experimental measurements indicate that the reduction in grain size in the FCC phase with increasing true strain is more pronounced than in the BCC phase. This is attributed to the initially larger grain size in the FCC phase, where the DRX effect is more significant. From 1100°C to 1200°C, the grain size after DRX increases with temperature, with the average DRX grain sizes at a strain of 0.7 for the FCC phase being 16.8 μm, 23.7 μm, and 30.3 μm, respectively.

A similar correlation between temperature and recrystallized grain size is also observed in the BCC phase in Fig.9(b). At 1150°C, the initial average grain size in the BCC phase is 23.7 μm, with about 67.5% of the grains having diameters below 25 μm. This size reduces to 10.9 μm at a strain of 0.2 and further to 9.6 μm at a strain of 0.7 after DRX, indicating a refinement degree of 40.5%, which confirms that the impact of DRX is weaker on the BCC phase, which inherently has smaller grains. At other temperatures, the average DRX grain sizes in the BCC phase do not significantly decrease at a strain of 0.2, with average DRX grain sizes at a strain of 0.7 being 9.1 μm and 9.94 μm, consistent with the phenomenon of increasing DRX grain size as temperature rises.

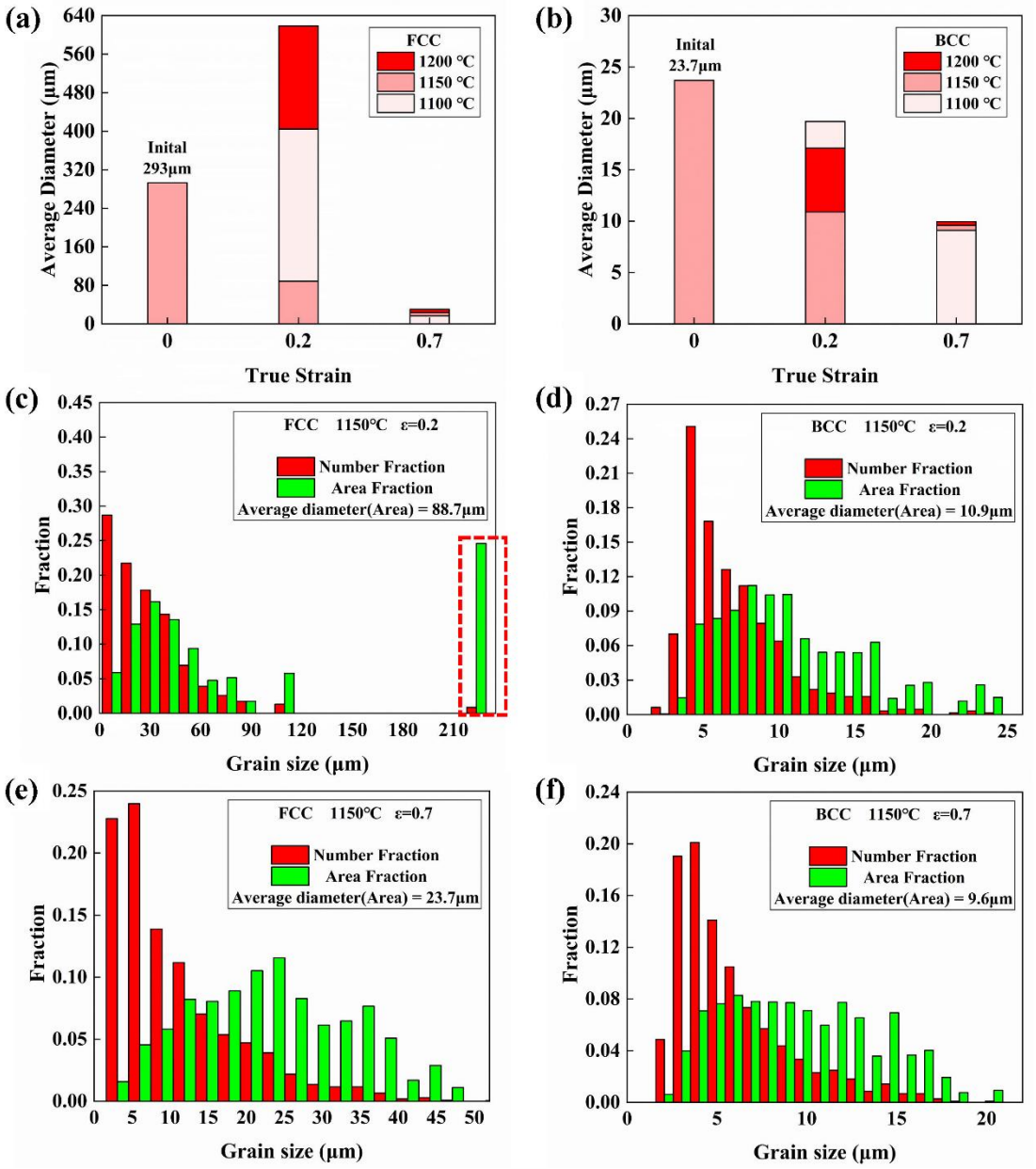

Fig 9 Grain size variations in (a, b) FCC and BCC Phases at 1100°C, 1150°C, and 1200°C; Grain size changes for (a) the FCC phase and (b) the BCC phase at temperatures of 1100°C, 1150°C, and 1200°C. Grain sizes of (c) the FCC phase and (b) the BCC phase at 1150°C with ε = 0.2. Grain sizes of (e) the FCC phase and (f) the BCC phase at 1150°C with ε = 0.7.

It is noteworthy that in Fig.9(c), the distribution of FCC grain sizes at a strain of 0.2 shows that a majority of grains have not undergone refinement, with sizes remaining above 210 μm, indicating incomplete DRX at this stage. This observation underscores how temperature influences the grain refinement induced by DRX, which is why stress decreases as temperature increases. Grain refinement is achieved through the formation of new nuclei and the consumption of old grains. At

higher temperatures, new nuclei form more easily and grow faster. As the number of new nuclei increases and the size of the grains decreases, the dislocation density within the crystal is reduced, thereby decreasing the stress concentration of the material and ultimately leading to a reduction in overall stress levels [57].

4.2.2 CPFEM simulation analysis

The impact of hot deformation temperatures on DRX, as well as the related mechanical properties and microstructural changes, can be simulated using CPFEM. In Fig. 10, the distribution of von Mises stress across different temperatures shows a decrease in stress values for both phases as the temperature increases, a phenomenon that is corroborated by the stress-strain curves presented in Fig. 6. Furthermore, at all temperatures, the stress values of the BCC phase are consistently higher than those of the FCC phase. Fig. 7(region P2) is discussed how under varying strain conditions at the same temperature, stress concentrations caused by slip bands at high strains replace those arising from uneven stress distributions due to phase stress. In the stress distribution plots at 1100°C, the stress difference between the slip bands and their edges is smaller than at 1200°C. This indicates that as the temperature increases, the stress values between the FCC and BCC phases converge more closely. The historically higher BCC/FCC stress ratio, caused by phase structures, gradually approaches unity and is replaced by stress concentrations induced by uneven slip deformation.

The distribution map of dislocation density shows that dislocation annihilation occurs in regions of high deformation, while accumulation of dislocation density occurs primarily near the BCC phase. This is attributed to phase boundaries that impede the movement of dislocations and cause them to accumulate at these boundaries. As strain increases, the overall dislocation density decreases, but the dislocation annihilation zones become more pronounced (see Fig. 7(a)). However, as the temperature increases, the phenomenon of dislocation annihilation weakens at the same strain level of 0.7, due to the dislocation density in the FCC phase not decreasing rapidly enough during the DRX process, maintaining a balance between dislocation generation and annihilation.

At any temperature, the grain refinement process in the FCC phase is stronger than in the BCC phase. Using the grain size of the FCC phase as the sole predictive indicator in the grain size distribution chart, it can be observed that the size of the DRX grains tends to increase with increasing temperatures, a phenomenon that corresponds to the experimental results. However, in areas of significant deformation, the grain sizes are significantly smaller than those in areas of lower strain,

with the difference being most pronounced at 1200°C.

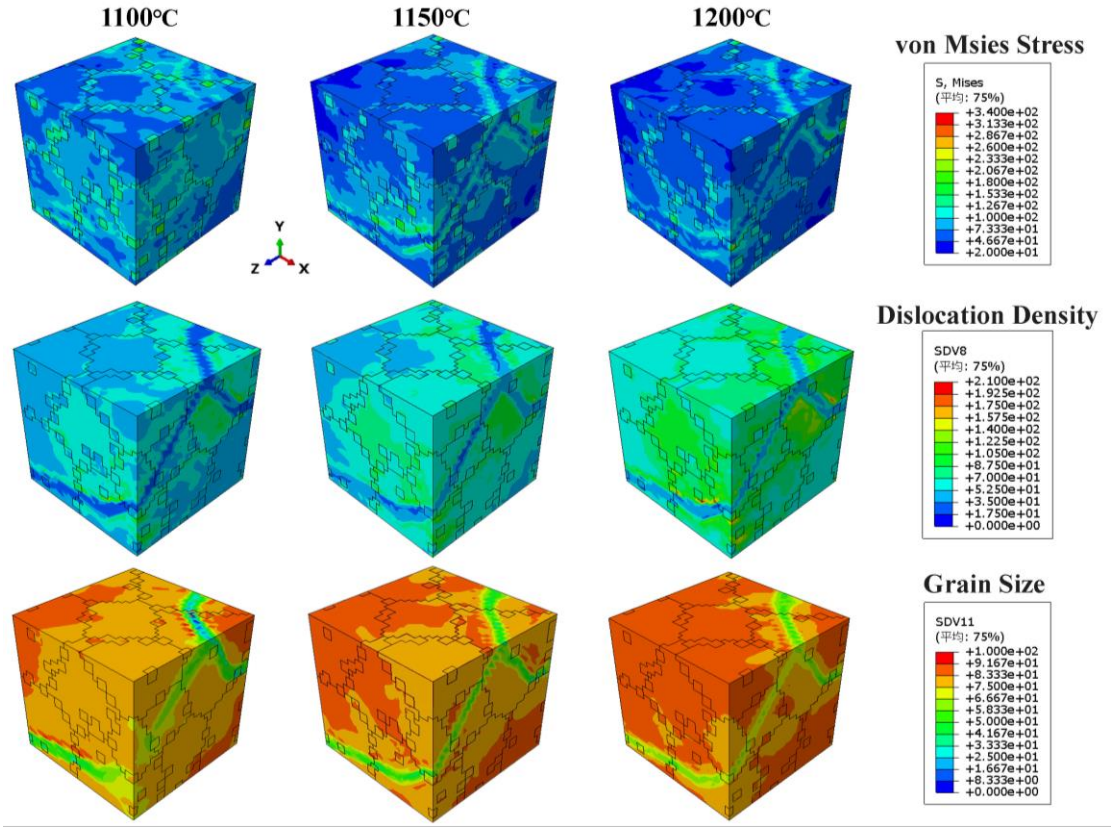

Fig. 10 Crystal plasticity simulation of von Mises stress, dislocation density, and grain size distribution at 1100°C, 1150°C, and 1200°C.

Higher temperatures increase the diffusion rate of the atoms, facilitating the rearrangement and annihilation of dislocations, which in turn promotes the recrystallisation and growth of grains, leading to a softening of the stress [58]. In areas of significant deformation, high stress and dislocation density reduce grain size, resulting in finer structures. Taking into account slip systems, dislocation dynamics, and grain interactions, the CPFEM model accurately captures the complex relationship between grain size, dislocation density, and stress. The high consistency of the model with experimental data confirms its precision in predicting the microstructural and mechanical behaviour of materials during hot deformation.

To better understand the relationship between mechanical responses and microstructural state variables, data points were taken from regions of high stress (slip bands) in the model. Fig.11 shows the von Mises stress, grain size, and dislocation density curves as a function of true strain.

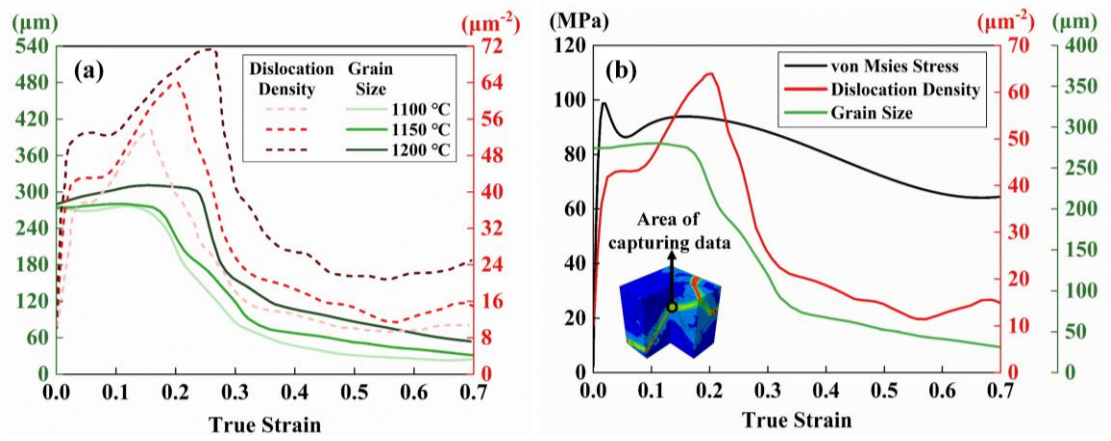

Fig. 11 (a) Curves of changes in dislocation density and grain size at different temperatures. (b) Curves of the relationship between von Mises stress, grain size, and dislocation density with true strain at 1150°C.

Figure 11(a) illustrates the effects of hot deformation temperatures on dislocation density and grain size. The model's predictions of grain size changes align with experimental results, showing an increase in DRX grain size with increasing temperatures. Consequently, the dislocation density increases with temperature, and the strain corresponding to the peak dislocation density shifts to higher values as the temperature increases. These observations confirm that the critical strain to initiate the DRX process varies with temperature.

When plastic deformation begins and stress collapse has not yet occurred, the grain size remains stable because DRX has not yet begun, and at this stage, the dislocation density shows almost linear growth during the stress recovery phase following initial recrystallisation. As true strain increases, the collapse of stress signals the onset of DRX, leading to a rapid decrease in both grain size and dislocation density, with dislocation annihilation lagging behind the reduction in grain size, as illustrated in Fig. 11(b). In particular, according to the Hall-Petch law, the flow stress should increase when the grain size decreases due to DRX [59]. However, in this study, stress consistently shows a softening, which is due to the softening mechanisms from intense dislocation annihilation during DRX outweighing the hardening effects of grain refinement[57], resulting in a concurrent downward trend in stress, dislocation density, and grain size.

4.3 Influence of DRX on deformation behavior: Interactions with GBs and texture evolution

4.3.1 GBs and DRX mechanisms in dual phase

It is well known that DRX plays a crucial role in the high-temperature deformation of HEA.

The occurrence of DRX gradually replaces grains under high stress with those under lower stress, effectively reducing the deformation forces in HEA and resulting in material softening. Additionally, different DRX mechanisms have varying impacts on GBs.

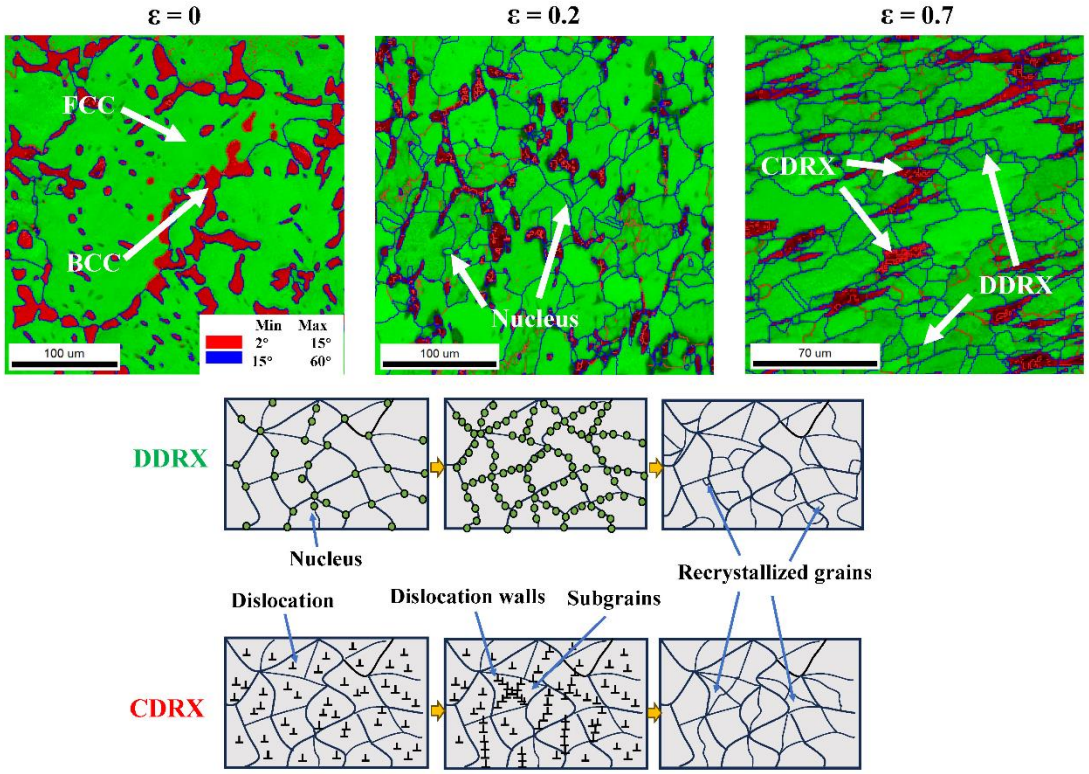

Fig 12 GB maps in different phases for ε = 0 , 0.2 and 0.7 and schematic illustration of the DDRX and CDRX mechanisms.

Figure 12 presents a GB map after hot deformation, distinguishing the FCC and BCC phases with two different colours. During the deformation process, it is evident that high-angle grain boundaries (HAGBs, >15°, shown with red lines) and low-angle grain boundary clusters (LAGB, 2-15°, shown with blue lines) appear, with most LAGBs densely forming within the grains of the BCC phase. Under high-temperature deformation, strain-induced dislocations are polygonized to form recovery subgrains. Dislocation networks on adjacent subgrain boundaries, which have small orientation angles, can dissociate, separate, and migrate to other subgrain boundaries, thus facilitating the merging of subgrains. These newly formed subgrain boundaries absorb dislocations and gradually transform LAGBs into HAGBs, thereby forming DRX. This is a typical characteristic of continuous dynamic recrystallisation (CDRX)[60], as illustrated in the schematic in Fig.12. This indicates that the predominant recrystallisation mechanism in the BCC phase is CDRX.

In metals with low or medium stacking fault energy (SFE), the main recrystallisation

mechanism is DDRX [60]. Its characteristics include slow grain growth; when the critical strain is reached, new grains form along GBs, triple junctions, and phase boundaries, leading to the formation of new DRX grains with HAGBs. The "necklace" nucleation and the low SFE in the FCC phase of HEAs found in other studies[61-63] indicate that DDRX is the predominant active mechanism during the hot deformation process of the FCC phase. This also explains why the DRX softening and grain refinement processes are not consistent between the two phases.

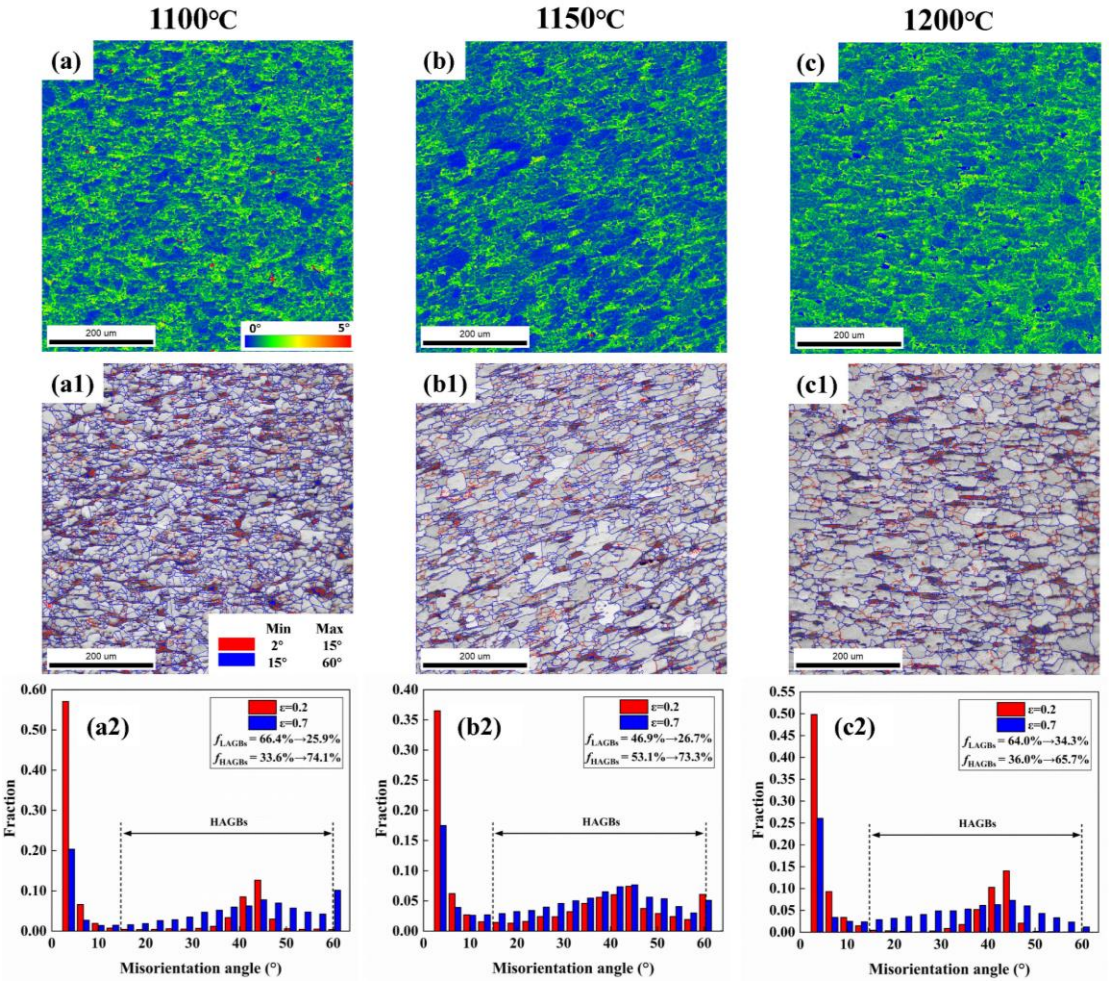

Fig 13 KAM diagrams of Ni61Fe10Cr10Al17Mo2 HEA after deformation at (a) 1100°C, (b) 1150°C, and (c)1200°C. The GB maps at (a1) 1100°C, (b1) 1150°C, and (c1)1200°C. Corresponding misorientation distributions for ε = 0.2 and 0.7 at (a2) 1100°C, (b2) 1150°C, and (c2)1200°C.

While the different SFE in the FCC and BCC phases might be one of the reasons affecting the DRX mechanism, variations in deformation temperature have also been suggested to lead to transitions between DDRX and CDRX [64]. In Fig.13(a1), (b1), and (c1), GB maps at different temperatures are respectively depicted. Since HAGBs are gradually transformed from LAGBs,

HAGBs formed by CDRX are typically surrounded by LAGBs with MAGBs. (The orientation error range is 10° to 15°)[65]. Regardless of the temperature, clusters of misoriented LAGBs are found near HAGBs in the BCC phase. Meanwhile, in the FCC phase, HAGBs resulting from DRX grain nucleation still appear near GBs, indicating that DRX mechanisms do not vary with temperature. Additionally, the increase in DRX grain size during deformation is not commonly observed for DDRX. The DRX grains in the FCC phase do not exhibit significant growth, even after complete DRX at 1200°C, with grain sizes remaining below 35 μm (see Fig.9). These observations validate the effectiveness of the multiphase nature of Ni61Fe10Cr10Al17Mo2 HEA in inhibiting GB migration during DRX processes, leading to slow grain growth and reduced grain size.

As shown in Fig.13(a2), (b2), and (c2), with strain increases from 0.2 to 0.7, the proportion of HAGBs f_{HAGBs} at 1100°C increases from 33.6% to 74.1%, at 1150°C it increases from 53.1% to 73.3%, and at 1200°C it increases from 36% to 65.7%. f_{HAGBs} increases with increasing deformation at all temperatures, indicating that the influence of GBs increases with increasing volume fraction of DRX.

As temperature increases, f_{HAGBs} decreases after complete DRX, with the lowest impact of GBs observed at 1200°C, reflected in Fig.6 as the lowest stress during hot compression. Larger DRX grains indicate faster dislocation annihilation, suggesting a lower dislocation density. However, in the KAM map, the dislocation density at 1200°C is larger. Combining this phenomenon with the increase in f_{LAGBs} with rising temperature, it can be inferred that subgrain boundary generation within newly formed DRX grains. The CPFEM simulations support this observation (see Fig. 11).

4.3.2 Texture evolution of the FCC and BCC phases

DRX can influence the macroscopic texture of materials and alter subsequent deformation behaviour. Fig. 14 shows experimental and simulated PFs of different phases with a strain of 0.7 for orientations (001), (011) and (111). The robust alignment between the simulated and experimental textures validates the model's ability to accurately predict the texture evolution of Ni61Fe10Cr10Al17Mo2 HEA during high-temperature deformation processes. Furthermore, the initiation of DRX at a strain of 0.7 not only decreases the texture strength, but also systematically organises the crystal orientations within the deformed structure. Among these, in the (111) PF of the FCC phase, a typical Goss texture {110}<100> appears. This is due to the activity of the {111}<110> slip system, where unstable crystal orientations gradually rotate toward the stable <111> and <001>

directions, which have high and low Taylor factors, respectively. This rotation contributes to the development of the Goss texture. In the BCC phase, a multitude of random orientations form, resulting in a more complex texture. This complexity is attributed to the activity of various slip systems[12].

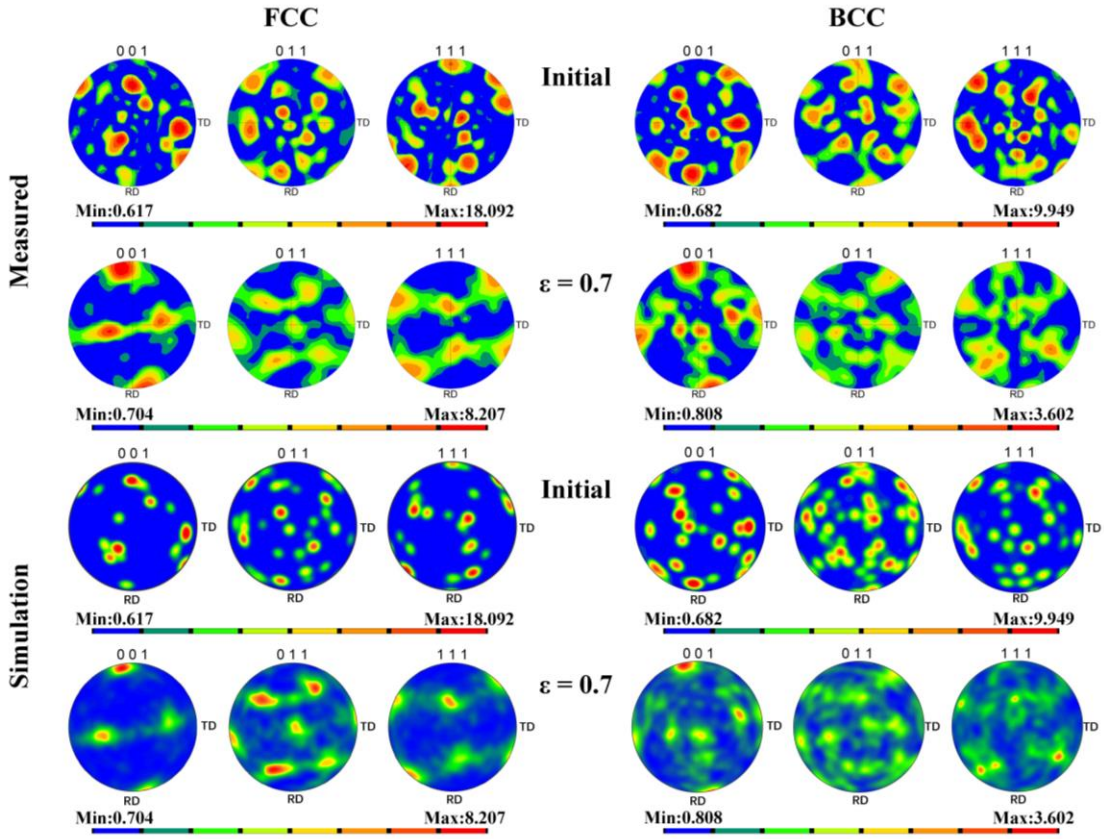

Fig 14 Comparisons of the experimental and simulated (001), (011) and (111) PFs of Ni61Fe10Cr10Al17Mo2 HEA at 1150°C and ε = 0.7.

Texture significantly influences the evolution of yield strength and flow stress during hot compression processes. Due to differences in the activation capabilities of slip systems, various textures exhibit distinct soft and hard orientations during compression deformation. For example, grains with Cube texture {100}<001> display a softer response, while those with Goss {110}<100> and Brass {110}<112> textures reveal stiffer response [29,66]. Fig.15 further illustrates changes in texture at different temperatures; the texture strength of the FCC phase increases with temperature, reaching 8.491 at 1200°C. The original Goss texture {110}<100> transitions to the more stable Cube texture {100}<001>. This transition reveals that as the deformation temperature increases, DRX accelerates the evolution of the alloy's crystal structure, effectively eliminating some of the textural heterogeneity caused by deformation.

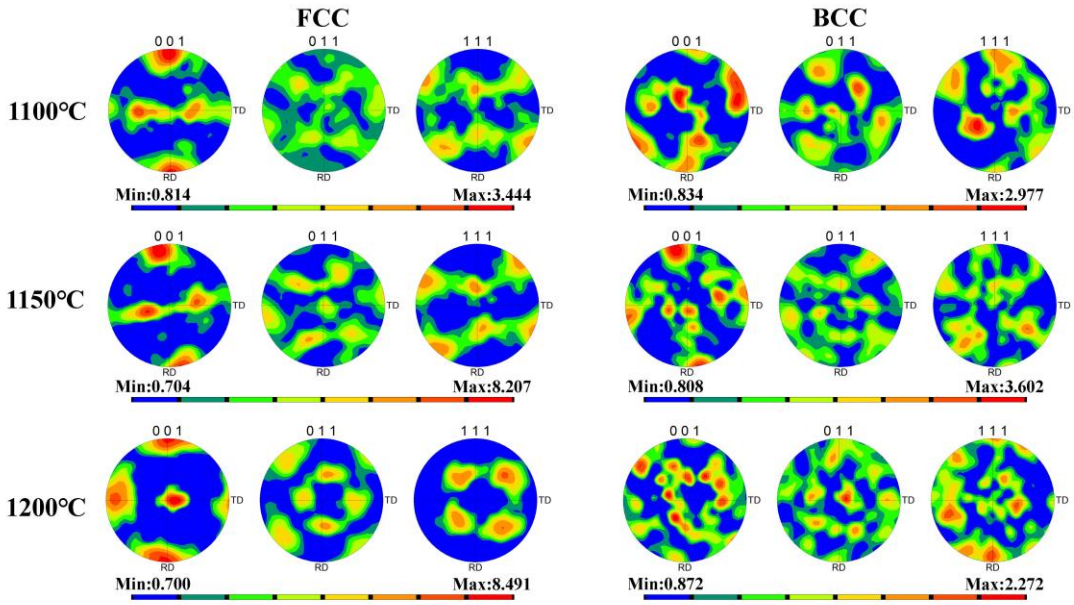

Fig 15 Comparison of (001), (011) and (111) PFs for deformed texture at different temperatures and $\varepsilon = 0.7$.

5. Conclusions

This study analysed the behaviour of DRX in dual-phase HEAs under high temperature compression between 1100 to 1200°C and its impact on flow stress and microstructural organisation. The evolution of microstructures at strains of 0.2 and 0.7 was thoroughly examined, and differences in stress response and DRX mechanisms between FCC and BCC phases were analysed. Additionally, a material model for dual-phase HEA was developed in a CPFEM framework to predict the stress softening and grain size changes caused by DRX, further enhancing our understanding of the impact of DRX behavior in dual-phase HEAs. The main conclusions of this work are as follows:

1、 At low strain, stress concentrations in Ni61Fe10Cr10Al17Mo2 HEA occur at phase boundaries due to higher stress in the BCC phase encircling the FCC phase. At 0.7 strain, stress concentrates in slip bands, replacing the dual-phase boundary stress distributions.

2、 The degree of DRX f_{DRX} is highest at 1150°C being 53.1%. The DRX grain size increase with rising temperature. In the FCC phase, the average size of the DRX grains is largest at 1200°C, measuring 30.3 μm.

3、 A crystal plasticity model for dual phase HEA has been established, which can effectively

predict the evolution of stress and microstructure. This model incorporating the DRX and its effects on dislocation structure, grain size and crystallographic texture has promising potentials for further applications that involve thermomechanical processes or applications.

4、 The rate of DRX evolution differs between the two phases, with minimal growth after the DRX grains are fully refined. This is attributed to the multiphase nature of the Ni61Fe10Cr10Al17Mo2 HEA and the dominant recrystallisation mechanisms: DDRX mainly in the 90% FCC phase and CDRX in the BCC phase.

5、 The Goss texture {110}<100> is a principal texture of the FCC phase, with its texture strength increasing as the temperature increases. However, when the temperature reaches 1200°C, the Goss texture {110}<100> transitions to the Cube texture {100}<001>.

CRediT authorship contribution statement

Zi-xin Zhou: Software, Methodology, Investigation, Data curation, Writing – original draft. **Yuan-ming Huo:** Conceptualization, Project administration, Funding acquisition, Writing – review & editing. **Zhi-jun Wang:** Resources, Supervision, Project administration. **Eralp Demir:** Software, Validation, Writing –review & editing. **Anqi Jiang:** Software. **Zhen-rong Yan:** Writing –review & editing. **Tao He:** Writing –review & editing.

Declaration of Competing Interest

All participating authors declare that they have no conflict of interest in this work. We once again solemnly declare that there is no conflict of interest with the submitted work, such as commercial interest or ancillary interest.

Data availability

Data will be made available on request.

Acknowledgements

This work was supported by the National Natural Science Foundation of China (Grants No. 51874245) and the National Natural Science Foundation of Shaanxi Province in China (2020JQ-720).

References

[1] Z. Yong, Z. Ting Ting, T. Zhi, et al., Microstructures and properties of high-entropy alloys, Progress in Materials Science, 61 (2014) 1-93, https://doi.org/10.1016/j.pmatsci.2013.10.001.

[2] B. Cantor, I.T.H. Chang, P. Knight, et al., Microstructural development in equiatomic multi component alloys, Materials Science and Engineering: A, 375-377 (2004) 213-218, https://doi.org/10.1016/j.msea.2003.10.257.

[3] Z. Li, S. Zhao, H. Diao, et al., High-velocity deformation of Al0.3CoCrFeNi high-entropy alloy: Remarkable resistance to shear failure, Scientific Reports, 7 (2017) 42742, https://doi.org/10.1038/srep42742.

[4] R. Soler, A. Evirgen, M. Yao, et al., Microstructural and mechanical characterization of an equiatomic YGdTbDyHo high entropy alloy with hexagonal close-packed structure, Acta Materialia, 156 (2018) 86-96, https://doi.org/10.1016/j.actamat.2018.06.010.

[5] G. Sindhura, G. Bharat, S. Vishal, et al., Contrasting mechanical behavior in precipitation hardenable AlXCoCrFeNi high entropy alloy microstructures: Single phase FCC vs. dual phase FCC-BCC, Materials Science and Engineering: A, 739 (2019) 158-166, https://doi.org/10.1016/j.msea.2018.10.021.

[6] L. Jianlin, Z. Ge, H. Jinke, et al., Special hot working plastic deformation behavior and microstructure evolution mechanism of single-phase BCC structure AlFeCoNiMo0.2 high-entropy alloy, Journal of Alloys and Compounds, 955 (2023) 170149, https://doi.org/10.1016/j.jallcom.2023.170149.

[7] L. Jianlin, Z. Ge, H. Jinke, et al., Dynamic recrystallization behavior of single-phase BCC structure AlFeCoNiMo0.2 high-entropy alloy, Journal of Materials Research and Technology, 23 (2023) 4376-4384, https://doi.org/10.1016/j.jmrt.2023.02.074.

[8] P. Shi, W. Ren, T. Zheng, et al., Enhanced strength–ductility synergy in ultrafine-grained eutectic high-entropy alloys by inheriting microstructural lamellae, Nature Communications, 10 (2019) 489, https://doi.org/10.1038/s41467-019-08460-2.

[9] Y. Jia, Z. Wang, Q. Wu, et al., Enhancing the yield strength of Ni–Co–Cr–Fe–Al as-cast hypoeutectic high-entropy alloys by introducing γ′ precipitation, Materials Science and Engineering: A, 858 (2022) 144190, https://doi.org/10.1016/j.msea.2022.144190.

[10] M. Huang, J. Jiang, Y. Wang, Deformation behavior, microstructure evolution, phase transformation and plastic instability origin of powder metallurgy Al0.8Co0.5Cr1.5CuFeNi alloy during high temperature deformation, Materials Science and Engineering: A, 861 (2022) 144373, https://doi.org/10.1016/j.msea.2022.144373.

[11] W. Zhang, P.K. Liaw, Y. Zhang, Science and technology in high-entropy alloys, Science China Materials, 61 (2018) 2-22, https://doi.org/10.1007/s40843-017-9195-8.

[12] M.H. Asoushe, A.Z. Hanzaki, H.R. Abedi, et al., Thermal stability, microstructure and texture evolution of thermomechanical processed AlCoCrFeNi2.1 eutectic high entropy alloy, Materials Science and Engineering: A, 799 (2021) 140012, https://doi.org/10.1016/j.msea.2020.140012.

[13] J. Charkhchian, A. Zarei-Hanzaki, T.M. Schwarz, et al., Unleashing the microstructural evolutions during hot deformation of as-cast AlCoCrFeNi2.1 eutectic high entropy alloy, Intermetallics, 168 (2024) 108253, https://doi.org/10.1016/j.intermet.2024.108253.

[14] R.H. Buzolin, M. Masswohl, F.M. Branco Ferraz, et al., Hot deformation mechanisms of dual phase high entropy alloys, Materials Science and Engineering: A, 878 (2023) 145235, http

s://doi.org/10.1016/j.msea.2023.145235.
[15] B.-R. Chen, A.-C. Yeh, J.-W. Yeh, Effect of one-step recrystallization on the grain boundary evolution of CoCrFeMnNi high entropy alloy and its subsystems, Scientific Reports, 6 (2016) 22306, https://doi.org/10.1038/srep22306.
[16] X. Jiang, X. Che, G. Zhou, et al., Study on thermal deformation constitutive model of NiCoFeAlCrMo high-entropy alloy with FCC L12 coherent structure, Materials Today Communications, 38 (2024) 107757, https://doi.org/10.1016/j.mtcomm.2023.107757.
[17] R. Guo, P. Zhang, J. Pan, et al., Achieving prominent high-temperature mechanical properties in a dual-phase high-entropy alloy: A synergy of deformation-induced twinning and martensite transformation, Acta Materialia, 264 (2024) 119591, https://doi.org/10.1016/j.actamat.2023.119591.
[18] H.T. Jeong, H.K. Park, W.J. Kim, Dynamic recrystallization and hot deformation mechanisms of a eutectic Al0.7CoCrFeMnNi high-entropy alloy, Journal of Alloys and Compounds, 871 (2021) 159488, https://doi.org/10.1016/j.jallcom.2021.159488.
[19] N.D. Stepanov, D.G. Shaysultanov, N.Y. Yurchenko, et al., High temperature deformation behavior and dynamic recrystallization in CoCrFeNiMn high entropy alloy, Materials Science and Engineering: A, 636 (2015) 188-195, https://doi.org/10.1016/j.msea.2015.03.097.
[20] J. Wang, J. Zhao, Y. Jia, et al., Hot deformation behavior of Ni61Fe10Cr10Al17Mo2 high-entropy alloy with hierarchical structure, Journal of Materials Research and Technology, 26 (2023) 6041-6052, https://doi.org/10.1016/j.jmrt.2023.08.303.
[21] P. Gao, M. Fu, M. Zhan, et al., Deformation behavior and microstructure evolution of titanium alloys with lamellar microstructure in hot working process: A review, Journal of Materials Science & Technology, 39 (2020) 56-73, https://doi.org/10.1016/j.jmst.2019.07.052.
[22] M.R. Rahul, S. Sumanta, S. Venugopal, et al., Experimental and finite element simulation studies on hot deformation behaviour of AlCoCrFeNi2.1 eutectic high entropy alloy, Journal of Alloys and Compounds, 749 (2018) 1115-1127, https://doi.org/10.1016/j.jallcom.2018.03.262.
[23] Q. Ling, Z. Jingchuan, Unveiling the compressive behavior of Fe2Ni2CrAl high entropy alloy: A combined molecular dynamics and finite element study, Materials Today Communications, 34 (2023) 105296, https://doi.org/10.1016/j.mtcomm.2022.105296.
[24] T.J. Gao, D. Zhao, T.W. Zhang, et al., Strain-rate-sensitive mechanical response, twinning, and texture features of NiCoCrFe high-entropy alloy: Experiments, multi-level crystal plasticity and artificial neural networks modeling, Journal of Alloys and Compounds, 845 (2020) 155911, https://doi.org/10.1016/j.jallcom.2020.155911.
[25] X. Zhang, X. Lu, J. Zhao, et al., Temperature effect on tensile behavior of an interstitial high entropy alloy: Crystal plasticity modeling, International Journal of Plasticity, 150 (2022) 103201, https://doi.org/10.1016/j.ijplas.2021.103201.
[26] S. Gao, Y. Sun, Q. Li, et al., Research on the hot tensile deformation mechanism of Ti-6Al-4V alloy sheet based on the α + β dual phase crystal plasticity modeling, Journal of Alloys and Compounds, 932 (2023) https://doi.org/10.1016/j.jallcom.2022.167701.
[27] X. Lu, J. Zhao, C. Yu, et al., Cyclic plasticity of an interstitial high-entropy alloy: experiments, crystal plasticity modeling, and simulations, Journal of the Mechanics and Physics of Solids, 142 (2020) 103971, https://doi.org/10.1016/j.jmps.2020.103971.
[28] Y. Zhang, C. Yang, H. Ke, et al., A study on the microstructure and mechanical behavior of CoCrFeNi high entropy alloy fabricated via laser powder bed fusion: Experiment and crystal

plasticity finite element modelling, Materials Science and Engineering: A, 893 (2024) 146111, https://doi.org/10.1016/j.msea.2024.146111.
[29] W. An, C. Liu, Q. Xiong, et al., Shear localization in polycrystalline metal at high-strain rates with dynamic recrystallization: Crystal plasticity modeling and texture effect, International Journal of Plasticity, 165 (2023) 103616, https://doi.org/10.1016/j.ijplas.2023.103616.
[30] C. Hardie, D.J. Long, E. Demir, et al., A robust and efficient hybrid solver for crystal plasticity, International Journal of Plasticity, 170 (2023) 103773, https://doi.org/10.1016/j.ijplas.2023.103773.
[31] R.J. Asaro, J.R. Rice, Strain localization in ductile single crystals, Journal of the Mechanics and Physics of Solids, 25 (1977) 309-338, https://doi.org/10.1016/0022-5096(77)90001-1.
[32] S.R. Kalidindi, C.A. Bronkhorst, L. Anand, Crystallographic texture evolution in bulk deformation processing of FCC metals, Journal of the Mechanics and Physics of Solids, 40 (1992) 537-569, https://doi.org/10.1016/0022-5096(92)80003-9.
[33] E. Orowan, Problems of plastic gliding, Proceedings of the Physical Society, 52 (1940) 8, https://doi.org/10.1088/0959-5309/52/1/303.
[34] U.F. Kocks, H. Mecking, Physics and phenomenology of strain hardening: the FCC case, Progress in Materials Science, 48 (2003) 171-273, https://doi.org/10.1016/S0079-6425(02)00003-8.
[35] H. Mark, M. Polanyi, E. Schmid, Vorgänge bei der Dehnung von Zinkkristallen, Zeitschrift für Physik, 12 (1923) 58-77, https://doi.org/10.1007/BF01328082.
[36] F.P.E. Dunne, D. Rugg, A. Walker, Lengthscale-dependent, elastically anisotropic, physically-based hcp crystal plasticity: Application to cold-dwell fatigue in Ti alloys, International Journal of Plasticity, 23 (2007) 1061-1083, https://doi.org/10.1016/j.ijplas.2006.10.013.
[37] F. Roters, P. Eisenlohr, L. Hantcherli, et al., Overview of constitutive laws, kinematics, homogenization and multiscale methods in crystal plasticity finite-element modeling: Theory, experiments, applications, Acta Materialia, 58 (2010) 1152-1211, https://doi.org/10.1016/j.actamat.2009.10.058.
[38] E.O. Hall, The Deformation and Ageing of Mild Steel: III Discussion of Results, Proceedings of the Physical Society. Section B, 64 (1951) 747, https://doi.org/10.1088/0370-1301/64/9/303.
[39] H. Mecking, U.F. Kocks, Kinetics of flow and strain-hardening, Acta Metallurgica, 29 (1981) 1865-1875, https://doi.org/10.1016/0001-6160(81)90112-7.
[40] U. Essmann, H. Mughrabi, Annihilation of dislocations during tensile and cyclic deformation and limits of dislocation densities, Philosophical Magazine A, 40 (1979) 731--756, https://doi.org/10.1080/01418617908234871.
[41] K. Huang, R.E. Logé, A review of dynamic recrystallization phenomena in metallic materials, Materials & Design, 111 (2016) 548-574, https://doi.org/10.1016/j.matdes.2016.09.012.
[42] D. Rittel, A.A. Kidane, M. Alkhader, et al., On the dynamically stored energy of cold work in pure single crystal and polycrystalline copper, Acta Materialia, 60 (2012) 3719-3728, https://doi.org/10.1016/j.actamat.2012.03.029.
[43] M.A. Groeber, M.A. Jackson, DREAM.3D: A Digital Representation Environment for the Analysis of Microstructure in 3D, Integrating Materials and Manufacturing Innovation, 3 (2014) 56-72, https://doi.org/10.1186/2193-9772-3-5.
[44] B. Yan, S. Jiang, L. Hu, et al., Crystal plasticity finite element simulation of NiTi shape

memory alloy under canning compression based on constitutive model containing dislocation density, Mechanics of Materials, 157 (2021) 103830, https://doi.org/10.1016/j.mechmat.2021.103830.
[45] K.-S. Zhang, J.W. Ju, Z. Li, et al., Micromechanics based fatigue life prediction of a polycrystalline metal applying crystal plasticity, Mechanics of Materials, 85 (2015) 16-37, https://doi.org/10.1016/j.mechmat.2015.01.020.
[46] H. Lim, C.C. Battaile, J.E. Bishop, et al., Investigating mesh sensitivity and polycrystalline RVEs in crystal plasticity finite element simulations, International Journal of Plasticity, 121 (2019) 101-115, https://doi.org/10.1016/j.ijplas.2019.06.001.
[47] E. Demir, E.W. Horton, M. Mokhtarishirazabad, et al., Grain size and shape dependent crystal plasticity finite element model and its application to electron beam welded SS316L, Journal of the Mechanics and Physics of Solids, 178 (2023) 105331, https://doi.org/10.1016/j.jmps.2023.105331.
[48] Y. Wang, B. Liu, K. Yan, Probing deformation mechanisms of a FeCoCrNi high-entropy alloy at 293 and 77 K using in situ neutron diffraction, Acta Materialia, 154 (2018) 79-89, https://doi.org/10.1016/j.actamat.2018.05.013.
[49] M.L. Ali, E. Haque, M.Z. Rahaman, Pressure- and temperature-dependent physical metallurgy in a face-centered cubic NiCoFeCrMn high entropy alloy and its subsystems, Journal of Alloys and Compounds, 873 (2021) 159843, https://doi.org/10.1016/j.jallcom.2021.159843.
[50] W. Li, Q. Gao, J. Ren, et al., Designing the composition and optimizing the mechanical properties of non-equiatomic FeCoNiTi high-entropy alloys, Journal of Materials Research and Technology, 29 (2024) 376-385, https://doi.org/10.1016/j.jmrt.2024.01.111.
[51] Y. Li, Y. Zhang, Z. Chen, et al., Hot deformation behavior and dynamic recrystallization of GH690 nickel-based superalloy, Journal of Alloys and Compounds, 847 (2020) 156507, https://doi.org/10.1016/j.jallcom.2020.156507.
[52] X.L. Liu, Q.Q. Xue, W. Wang, Back-stress-induced strengthening and strain hardening in dual-phase steel, Materialia, 7 (2019) 100376, https://doi.org/10.1016/j.mtla.2019.100376.
[53] J. Li, L. Jin, F. Wang, Microscopic and mesoscopic deformation behaviors of dual-phase Mg-Li-Gd alloys, Journal of Materials Science & Technology, 194 (2024) 1-15, https://doi.org/10.1016/j.jmst.2023.12.064.
[54] A. Marano, L. Gélébart, S. Forest, FFT-based simulations of slip and kink bands formation in 3D polycrystals: Influence of strain gradient crystal plasticity, Journal of the Mechanics and Physics of Solids, 149 (2021) 104295, https://doi.org/10.1016/j.jmps.2021.104295.
[55] T. Sakai, A. Belyakov, H. Miura, Ultrafine Grain Formation in Ferritic Stainless Steel during Severe Plastic Deformation, Metallurgical and Materials Transactions A, 39 (2008) 2206-2214, https://doi.org/10.1007/s11661-008-9556-8.
[56] K. Santosh, S. Dipti, B. Aashranth, et al., Dependency of rate sensitive DRX behaviour on interstitial content of a Fe-Cr-Ni-Mo alloy, Materials Science and Engineering: A, 743 (2019) 148-158, https://doi.org/10.1016/j.msea.2018.11.062.
[57] A. Shabani, M.R. Toroghinejad, M. Aminaei, et al., Dynamic recrystallization nanoarchitectonics of FeCrCuMnNi multi-phase high entropy alloy, Journal of Alloys and Compounds, 968 (2023) 172001, https://doi.org/10.1016/j.jallcom.2023.172001.
[58] H. Hedayat, A. Hamid Reza, Z. Yong, A review study on thermal stability of high entropy alloys: Normal/abnormal resistance of grain growth, Journal of Alloys and Compounds, 960 (2023) 170826, https://doi.org/10.1016/j.jallcom.2023.170826.

[59] D.J. Dunstan, A.J. Bushby, Grain size dependence of the strength of metals: The Hall–Petch effect does not scale as the inverse square root of grain size, International Journal of Plasticity, 53 (2014) 56-65, https://doi.org/10.1016/j.ijplas.2013.07.004.
[60] C. Tao, G. Zhou, H. Huang, et al., Research on energy dissipation and dynamic recrystallization microstructure evolution behavior of NiTi alloy during hot deformation, Materials Characterization, 208 (2024) 113673, https://doi.org/10.1016/j.matchar.2024.113673.
[61] E.P. George, W.A. Curtin, C.C. Tasan, High entropy alloys: A focused review of mechanical properties and deformation mechanisms, Acta Materialia, 188 (2020) 435-474, https://doi.org/10.1016/j.actamat.2019.12.015.
[62] J. Lu, W. Xin, T. Ma, et al., Hot deformation behavior and dynamic recrystallization of dual-phase (CrCoNi)94Al3Ta3 medium entropy alloy, Journal of Alloys and Compounds, 968 (2023) 172215, https://doi.org/10.1016/j.jallcom.2023.172215.
[63] J. Ren, M. Wu, C. Li, et al., Deformation mechanisms in an additively manufactured dual-phase eutectic high-entropy alloy, Acta Materialia, 257 (2023) 119179, https://doi.org/10.1016/j.actamat.2023.119179.
[64] H. Gao, B. Zhang, Y. Fan, et al., Study on the hot deformation behavior and microstructure evolution of as-forged GH3625 alloy, Journal of Materials Research and Technology, 30 (2024) 197-209, https://doi.org/10.1016/j.jmrt.2024.03.060.
[65] Y. Wang, G. Zhao, L. Sun, et al., Effects of strain and strain rate on dynamic recrystallization and solid-state welding behaviors of aluminum alloys, Journal of Materials Research and Technology, 29 (2024) 4036-4051, https://doi.org/10.1016/j.jmrt.2024.02.138.
[66] P. James, B. Soran, Crystallographic orientation influence on slip system activation and deformation mechanisms in Waspaloy during in-situ mechanical loading, Journal of Alloys and Compounds, 865 (2021) 158548, https://doi.org/10.1016/j.jallcom.2020.158548.